Experimental investigation of convective heat transfer for night ventilation in case of mixing ventilation

Guo, Rui; Heiselberg, Per; Hu, Yue; Johra, Hicham; Jensen, Rasmus Lund; Jønsson, Kim Trangbæk; Peng, Pei

Published in:
Building and Environment

DOI (link to publication from Publisher):
10.1016/j.buildenv.2021.107670

Publication date:
2021

Document Version
Accepted author manuscript, peer reviewed version

Experimental investigation of heat transfer for night ventilation in case of mixing ventilation

Rui Guo*, Per Heiselberg, Yue Hu, Hicham Johra, Rasmus Lund Jensen, Kim Trangbæk Jønsson, Pei Peng

Department of the Built Environment, Aalborg University, Thomas Manns Vej 23, Aalborg 9220, Denmark

**Corresponding author email address: rgu@build.aau.dk*

ABSTRACT

The purpose of night ventilation (NV) is to improve building energy and thermal comfort performance. The key to accurately predicting NV performance is selecting the appropriate convective heat transfer coefficient (CHTC) at different surfaces of the built environment. The current CHTC correlations used in building energy simulation tools are limited and prevent accurate modeling of NV strategies. The building thermal mass activation is also an important factor to influence the efficiency of NV. A series of dynamic full-scale experiments with ten thermal mass distribution schemes, four air change rates per hour (ACH), and two inlet air temperatures was conducted to derive the CHTCs at test room surfaces during NV in case of mixing ventilation. The results show that the existing correlations did not accurately predict the CHTC for most cases. Therefore, the new surface-averaged CHTC correlations with inlet temperature as reference were developed for different thermal mass distribution schemes and ACH. Installing the thermal mass on one surface can significantly enhance its CHTC and affect the CHTC at other surfaces. The mean CHTC of the test room was independent of the inlet air temperature but increased together with ACH and thermal mass level of interior surfaces. Finally, the presence and locations of tables had limited influence on the CHTC at interior surfaces but reduced the mean CHTC.

KEYWORDS

Night ventilation; Mixing ventilation; Convective heat transfer coefficient; Thermal mass; Dynamic full-scale experiment

Nomenclature

Latin symbols

A	Area
c	Heat capacity
C	Constant
C_{P}	Specific heat capacity
E_{b}	Black body emissive power
F	View factor
g	Gravitational acceleration
h	Surface heat transfer coefficient
k	Air thermal conductivity
L	Characteristic length
q	Heat flux
Q	Heat flow
T	Temperature
u	Airflow speed
$\dot{V}$	Air volume flow rate

Greek symbols

Δ	Change in a variable
δ	Kronecker symbol
ε	Emissivity
ρ	Density
v	Air dynamic viscosity
β	Coefficient of thermal expansion
λ	Thermal conductivity

Subscript

conv	Convective
cond	Conductive
rad	Radiative
surf	Surface
i,*j*	Index for surface *i* and *j*

Acronyms

ACH	Air change rate per hour
AHU	Air handling unit
Ar	Archimedes number
BES	Building energy simulation
CFD	Computational fluid dynamics
CHTC	Convective heat transfer coefficient
Gr	Grashof number
LHS	Latin Hypercube Sampling
MCA	Monte Carlo analysis
NV	Night ventilation
Re	Reynolds number
Ri	Richardson number
Nu	Nusselt number

1 INTRODUCTION

1.1 Background

An emerging challenge at the design stage and during operation is the increasing cooling demand and overheating period in buildings, especially in commercial buildings [1]. Night ventilation (NV) is a promising way to reduce the cooling demand in buildings and provide better indoor thermal comfort. The basic concept of NV consists of utilizing the relatively cold ambient air at night by means of natural or mechanical force to cool down the indoor air and building elements that have stored excess heat during the daytime. The cooled building elements can then act as a heat sink during the occupied period of the next day to absorb the heat gains and reduce risks of overheating [2]. In past decades, many researchers have experimentally or numerically investigated the building performance improvement offered by NV [3–14]. However, architects and engineers still hesitate to adopt NV in building design due to the high uncertainty in predicting its performance by using building energy simulation (BES) tools.

One of the factors contributing to this problem is the complexity and diversity of NV flow rates, leading to inaccurate convective heat transfer coefficient (CHTC) at the interior surfaces of the built environment. The purpose of daytime cooling (e.g., air conditioning) is to maintain the indoor air temperature within a certain range. This type of system usually has limited airflow rates to avoid risks of draft. Unlike daytime cooling in office buildings, night cooling can employ a high air change rate per hour (ACH) up to 10 h^{-1} or more if applicable [15]. Therefore, accurate CHTC is more critical to predict night cooling performance rather than for daytime cooling performance. Previous research conducted a series of sensitivity analyses to demonstrate that the internal CHTC is a crucial parameter in energy and thermal comfort prediction for NV [16–18].

Since it is impossible to analyze the airflow around and in the building in detail for the yearly BES, the empirical correlations are used to calculate the CHTC. For the past 60 years, researchers have developed numerous CHTC correlations based on experiments or theoretical analyses [19–28]. However, most of these correlations were deduced from the flat plate or steady state full-scale experiments. They are thus only applicable under specific conditions of ventilation principles and airflow regimes. The inappropriate selection of CHTC correlations makes a difference in ventilation performance prediction. The CHTC correlations themselves may also result in high uncertainty in predicting building energy use when forced convection is considered. Beausoleil-Morrison [29] proposed comprehensive, adaptive CHTC correlations for mixed convection, which blended the natural and forced convection correlations from the literature. Nevertheless, it was observed that high uncertainty of 20 – 40% occurred in predicting heating and cooling energy use. Several studies [13][30][31] conducted dynamic full-scale experiments to investigate the heat transfer for NV with different air distribution systems (mixing ventilation, displacement ventilation, and wall-mounted attached ventilation). However, those studies only looked at the convective heat flow of different surfaces and were only based on one thermal mass distribution. Moreover, they did not focus on characterizing CHTC or developing CHTC correlation.

Another factor that may impede the application of NV is the thermal mass activation. The thermal mass capacity accumulates the heat gain in the daytime and determines the cooling potential for NV; in turn, the capacity to release the heat at night affects the NV performance [32]. If coupling the thermal mass activation with NV to achieve the best performance for office buildings, it is necessary to account for the amount and location of thermal mass. Goethals et al. [33] investigated the influence of different inlet and exhaust configurations as well as the thermal mass on the heat transfer of two mixed convection regimes. The results revealed that when the inlet was close to the floor with thermal mass (concrete tiles) rather than near the

ceiling, NV released 11% more heat. More convective heat flow occurred when the floor was installed with concrete titles. This study only calculated the convective heat flow of surfaces and investigated a limited set of eight designed cases, of which only four cases had night cooling. Apart from the thermal mass on the building elements, several studies investigated the impact of internal thermal mass (e.g., furniture) on the convective heat transfer. Wallentén [34] experimented on a full-scale with and without furniture (a desk, two chairs, and a small chest). It was found that the furniture had little effect on the convective heat transfer along with the window and wall around the window. Spitler et al. [22] compared the airflow of an empty room and a furnished room (one table and six chairs or two cabinets), indicating that the furniture impacted the flow. Those studies only investigated the heat transfer of some room interior surfaces rather than the indoor furniture. The impact of the amount of indoor furniture and its location on the heat transfer in the room needs further study. Besides, none of the researchers deduced the CHTC at the interior surfaces with thermal mass.

In BES tools, it is easy to consider the thermal mass capacity in the room interior surfaces by setting the construction composition in detail. Modeling the internal mass (particularly furniture) accurately is cumbersome due to the difficulty of measuring internal mass geometry and quantifying its amount [35]. One approach to modeling the internal mass in BES software is simplifying the internal mass as a virtual equivalent planar element (i.e., a horizontal and upward-facing surface) [36]. The internal mass is involved in the zone air heat balance and the longwave radiant exchange with other surfaces. If both sides of the internal mass exchange energy with the zone, the user should double the mass area. The BES software switches algorithms applicable to the horizontal upward-facing surface for the internal mass based on the flow regime. One possible way to accurately model the furniture in BES is by adopting the specific CHTC algorithm. However, no specific correlations for internal mass were founded in the existing studies.

1.2 Novelty and main contributions

Regarding the current state-of-the-art, this study proposes experimental research that focuses on heat transfer, especially the CHTC of night cooling with mixing ventilation. A series of dynamic full-scale experiments involving 48 designed cases with ten thermal mass distribution schemes, four ACH, and two inlet temperatures were conducted. The original contributions of this study are briefly summarized in the following:

1) The influence of ACH, inlet temperature, and thermal mass (especially the indoor furniture) distribution on the CHTC at surfaces and the mean CHTC of the test room were comprehensively investigated.

2) The experimental CHTCs with the inlet temperature or local air temperature as reference were deduced and compared with existing CHTC correlations.

3) New CHTC correlations tailored for NV were developed, which provides architects and engineers with possibilities to design or optimize the NV system.

The organization of this paper is as follows. Section 2 describes the experimental setup. Section 3 introduces the data analysis method for the derivation of CHTC, uncertainty analysis, and energy balance criteria. Section 4 presents CHTCs at different surfaces under different designed cases. Section 5 summarizes the conclusion and suggestions for future work.

2 EXPERIMENTAL DESCRIPTIONS

2.1 Hot box setup

The so-called “Large Guarded Hot Box” located in the Aalborg University laboratory was used as a guarded test chamber to conduct the dynamic full-scale experiment. The hot box in this study was designed and constructed based on the guarded hot box concept [37]. Fig. 1 shows the vertical sectional view of the hot box. It consisted of the upper zone, the test room, and the

guarding zone. A 12 mm wood panel separated the upper zone and test room. The upper zone was a plenum. The test room represents an office room with dimensions of 4.2 m (L)×3.6 m (W)×2.5 m (H). The guarding zone enclosed both the upper zone and the lower zone.

The original insulations between different zones of the hot box were made by a sandwich element (i.e., 15 mm wood panel + 225 mm expanded polystyrene + 15 mm wood panel). It should be noticed that the original insulation for the front side of the hot box was not the sandwich element but a combined element consisting of a 150 mm foam board and a 12 mm wood panel. Apart from the original insulation of the hot box, 50 mm foam boards (ρ=14.5 kg/m^3, C_p=1500 J/kg·K, λ=0.038 W/m·K) were installed on the test room interior surfaces for better insulation. Due to the open position of the door to the hot box, the back wall of the room was insulated with 100 mm foam boards. An air handling unit (AHU) recirculated the air in the guarding zone to keep the zone air temperature identical to the stable laboratory air temperature (22 °C). The temperature of 22 °C was also a representative temperature for an office at the end of the summer working day [38]. Another AHU provided the conditioned air to the test room through a rectangular inlet to simulate the NV and exhausted the room air away through a round outlet. The inlet was located in the middle-upper portion of the front wall with a size of 250 mm (W)×100 mm (H). The outlet was located in the bottom right corner of the front wall with a diameter of 215 mm. A 1000 W electrical heater located before the inlet was turned on to heat the conditioned air with predefined cooling temperature (e.g., 12°C) to 22 °C for creating the steady state for the test room and was turned off when NV started so that the inlet air temperature for the room can reach the predefined cooling temperature quicker than the temperature adjustment by AHU.

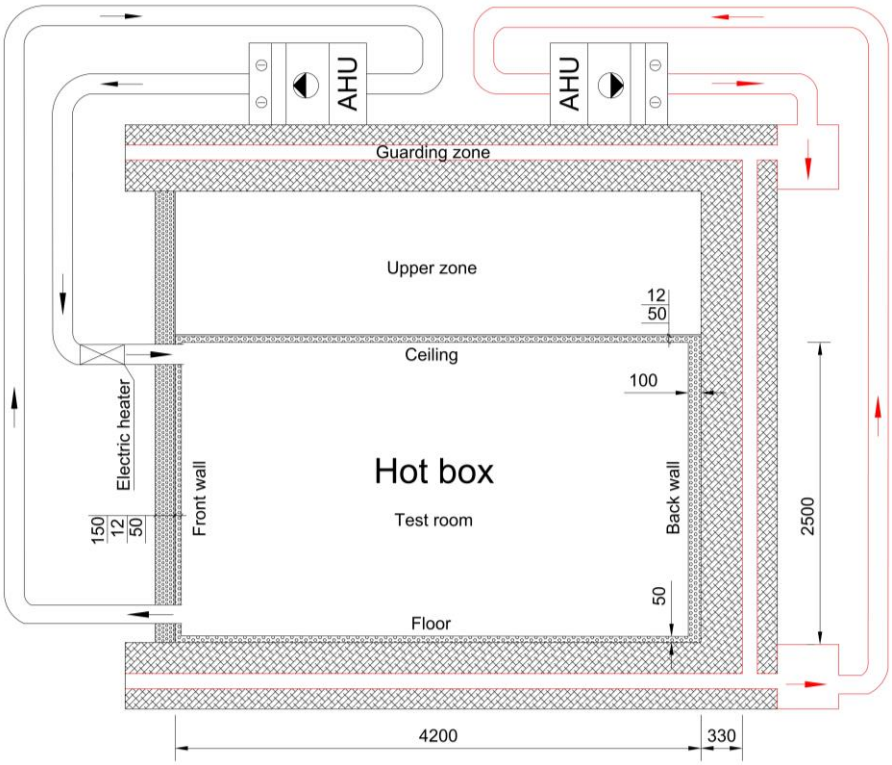

Fig. 1. Vertical section view of the hot box.

2.2 Measurement equipment and location of sensors

The measured parameters are temperatures, temperature differences between the interior (facing to the test room) and exterior surfaces, and air velocities. Table 1 presents the specification of the measurement equipment.

Table 1. Specification of the measurement equipment.

Equipment	Measured parameter	Range	Accuracy	Remark	Reference
FTMU UltraLink	Airflow rate	0 to 507 m^3/h	± 5%	Ø=160 mm	[39]
Type K thermocouple	Surface temperature Local, indoor, inlet, and outlet air temperature	0 to 50 °C	± 0.09 °C	-	[40]
PT 100	Supply air temperature, air temperature from AHUs	0 to 50 °C	± 0.1 °C	-	[41]
Thermopile	Temperature difference between interior and exterior surface	-	± 0.058 °C	Formed by three thermocouples connected in series	[42]

Hot-sphere anemometer	Air velocity	0 to 5 m/s	± 0.01 m/s	-	[43]

Each interior surface in the room was evenly divided into nine sections, and the center of each section was the measuring point for thermocouples or thermopiles (see Fig. 2a). All measuring points were coated with thermal paste to ensure good thermal contact between the temperature sensor and the surface. The temperature difference was used to calculate the conductive heat flux through the interior surface. Fig. 2b shows the location of the thermopile and thermocouple in a wall.

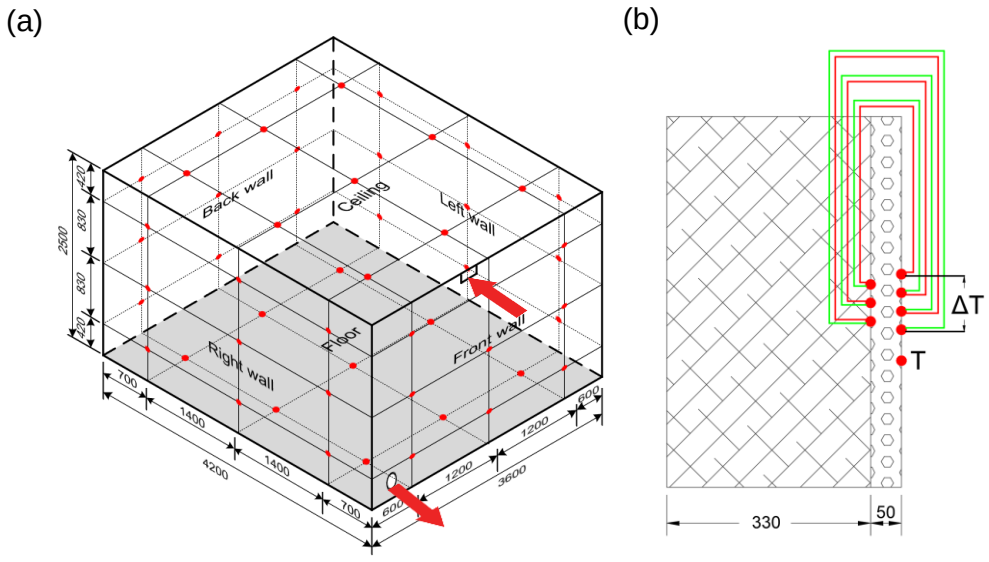

Fig. 2. (a) Positions of thermocouple/thermopile measuring points in interior surfaces, (b) the location of thermocouple and thermopile in a wall.

Hot-sphere anemometers were used to measure the local air velocities close to the interior surfaces for evaluating the flow regime near the surfaces. Some anemometers were fixed on the special movable columns labeled as "A1 – A13" in Fig. 3a or fixed close to the ceiling and floor of the test room labeled as "B1 – B9" in Fig. 3a. Twelve columns (A1 – A12) holding three anemometers were close to the internal walls with a 50 mm distance (see Fig. 3b). In addition, one column (A13) holding one anemometer was in the middle of the room (see Fig. 3c), and

the rest of the anemometers were located in the positions (B1 – B9) shown in Fig. 3d. It should be noticed that B9 and A13 were in the same position in the plan.

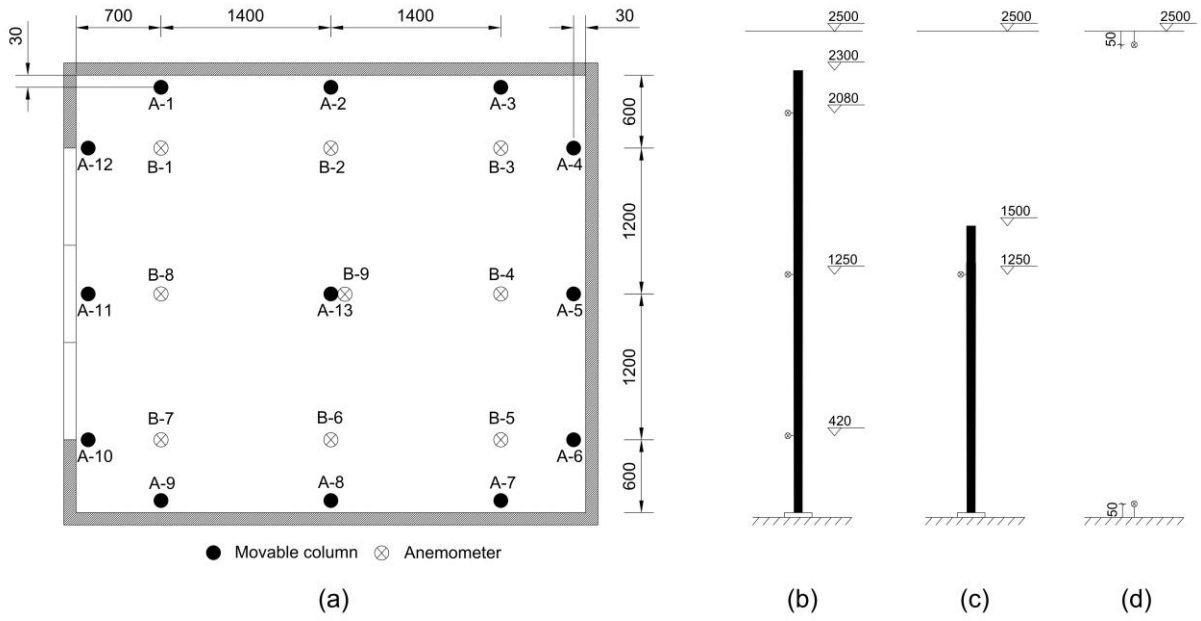

Fig. 3. (a) Horizontal positions of anemometers in the test room, (b) anemometers in the columns close to the room surface (A1-A12), (c) anemometer in the column in the middle of the room (A-13), (d) anemometers fixed close to the ceiling or floor (B1-B9).

The indoor air temperatures were measured by two thermocouples located in the middle of the test room and 1.2 m away from the floor. The inlet air temperatures and outlet air temperatures were measured by two thermocouples placed in the middle of the inlet (Fig. 4a) and outlet (Fig. 4b), respectively. The outlet was connected to an orifice with an FTMU UltraLink airflow sensor (Fig. 4c). All thermocouples and thermopiles were connected to two Fluke Helios Plus 2287A dataloggers. The conditioned air temperatures from AHUs were measured by PT 100 sensors. All the data was logged at a sampling rate of 0.1 Hz (every 10 s). The moving average of 15 values (2.5 min) was applied for temperature and temperature difference data to reduce the noise in the measurement signals.

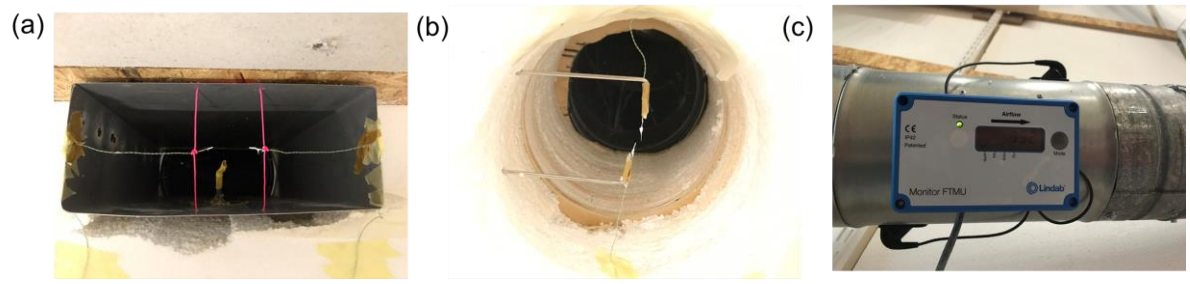

Fig. 4. Thermocouples for the (a) inlet, (b) outlet, and (c) orifice with airflow sensor.

2.3 Designed cases and experimental procedure

According to EN ISO 13786 [44], the dynamic heat capacity c_{dyn} defines the amount of energy that can be stored per surface area when the surface is exposed to a sinusoidal temperature variation with a 24 h period. The total dynamic heat capacity per unit floor area c_{dyn}/A_{floor} determines the building thermal mass level. The hot box construction described in Section 2.1 provided the test room with a low thermal mass level (c_{dyn}/A_{floor} = 37.8 kJ/m^2·K). To investigate the influence of thermal mass distribution on the surface heat transfer, 18mm fermacell® fiber plasterboards (ρ=1150 kg/m^3, C_p=1100 J/kg·K, λ=0.32 W/m·K) were installed on the different interior surfaces that were foam boards. Installing the fiber plasterboard increased the c_{dyn} of one original interior surface from 8.5 to 26.0 kJ/m^2·K. For the sake of simplification, the fiber plasterboard is called "thermal mass" in the following sections. Moreover, four tables assembled by the fiber plasterboards were also included to test different furniture distribution schemes. Each table contained two fiber plasterboards (of 36 mm thickness) and four metal columns. The height of the table was 700 mm. Fig. 5 shows the positions of indoor tables. Four air change rates per hour (ACH) and two initial temperature differences (ΔT_0) between the inlet and indoor air were set for different designed cases. Table 2 lists the designed cases and corresponding thermal mass level. The designed cases are referred to by abbreviations in later sections. For instance, '10 ACH 10 °C Ceiling+Floor' represents case 1, meaning that the ACH is 10 h^{-1}, ΔT_0 is 10 °C, and the thermal mass is installed on the ceiling and floor. It should be

noticed that the designed cases in Table 1 depended on initial trials and were updated based on primary results. The experiment started with the hypothesis that the initial temperature difference between the inlet and indoor air would make a difference for the CHTC. The preliminary results showed that the CHTCs (inlet temperature as reference) of the cases with the same ACH but different inlet temperatures were similar (cf. Section 4). It indicated that the initial temperature difference was not the case since the forced convection dominates during NV. Thus, the experiment only focused on the variation of ACH and thermal mass distribution.

The experiment procedures were: (1) supplying the air temperature with 22 °C until the steady state was reached (i.e., interior surfaces and indoor air temperature were close to 22 °C, the average temperature difference between the interior and exterior surfaces less than 0.1 °C) and (2) supplying the cold air continuously with the predefined temperature for eight hours to simulate NV. Steps 1 and 2 were then repeated for the next case.

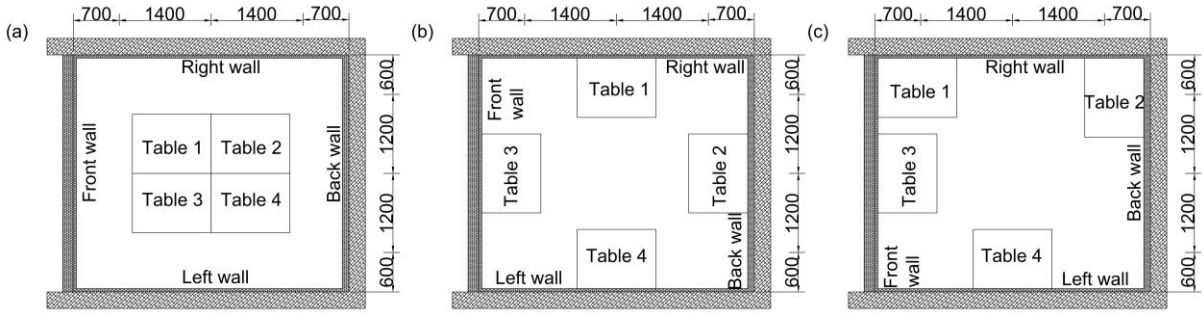

Fig. 5. Positions of tables (a) in the middle, (b) close to walls, and (c) close to the corners or the walls.

Table 2. Designed cases and the corresponding thermal mass level.

Case No.	Thermal mass distribution	ACH (h^{-1})	ΔT_0 (℃)	Total c_{dyn}/A_{floor} (kJ/m^2·K)
Case 1 to 8	Ceiling + Floor	10, 7, 5, 2	10, 5	72.2
Case 9 to 12	Ceiling + Floor + Table(a)	10, 7, 5, 2	10	97.5
Case 13 to 14	Ceiling + Floor + Table(a)	10, 5	5	97.5
Case 15 to 18	Ceiling + Floor + Table(b)	10, 7, 5, 2	10	97.5
Case 19 to 20	Ceiling + Floor + Table(b)	10, 5	5	97.5
Case 21 to 24	Ceiling + Floor + Table(c)	10, 7, 5, 2	10	97.5

Case 25 to 28	Ceiling + Floor + Right wall	10, 7, 5, 2	5	84.2
Case 29 to 32	Ceiling	10, 7, 5, 2	5	55.0
Case 33 to 36	Floor + Right wall	10, 7, 5, 2	5	67.0
Case 37 to 40	Floor	10, 7, 5, 2	5	55.0
Case 41 to 44	Right wall	10, 7, 5, 2	5	49.8
Case 45 to 48	Not installed	10, 7, 5, 2	5	37.8

3 METHODS OF DATA ANALYSIS

3.1 Derivation of CHTC

The CHTC is derived from the energy balance of the interior surface energy balance (see Fig. 6). The convective heat flux (q_{conv}) is equal to the difference of the conductive (q_{cond}) and radiative heat flux (q_{rad}). The CHTC for the surface *i* ($h_{\mathrm{conv},i}$) can thus be derived from Eq. (1). T_{ref} and $T_{\mathrm{surf},i}$ are the reference temperature and the surface *i* temperature, respectively.

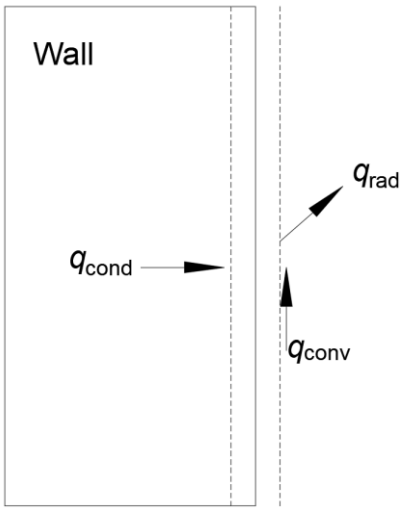

Fig. 6. The interior surface energy balance.

$$h_{\mathrm{conv},i} = \frac{q_{\mathrm{conv},i}}{(T_{\mathrm{ref}} - T_{\mathrm{surf},i})} \quad (1)$$

The conductive heat flux for each surface was calculated by a transient 1D finite-difference model with an explicit scheme [45]. The interior and exterior surface temperatures were used as boundary conditions for the finite-difference model. The exterior surface temperature was

calculated by subtracting the measured temperature difference between the interior and exterior surface from the measured interior surface temperature.

The radiosity method was chosen to calculate the radiative heat flow of each surface [46]. This method is based on the equivalent network of building construction to represent the interaction between surfaces and has been widely adopted in BES software like EnergyPlus and IDA-ICE.

$$\left[\frac{\delta_{ij}-(1-\varepsilon_i)\cdot F_{i-j}}{\varepsilon_i}\right][J_i] = [E_{\mathrm{b}i}] \tag{2}$$

$$q_{\mathrm{rad},i} = \frac{\varepsilon_i}{(1-\varepsilon_i)} \cdot [E_{\mathrm{b}i} - J_i] \tag{3}$$

where δ is the Kronecker symbol, ε is the emissivity, F_{i-j} is the view factor from surface i to surface j, and E_{b} is the black body emissive power. For the cases without tables, the view factors F_{i-j} between interior surfaces were determined according to [47]. For cases with tables, F_{i-j} between tables and other interior surfaces was calculated using the adaptive integration method [48].

3.2 Uncertainty analysis

To evaluate the accuracy of results, the uncertainty analysis was conducted by considering the accuracy of equipment (cf. Table 2) and the uncertainties of the material properties shown in Table 3. The material properties, excluding the emissivity, were given by the manufacturers. The material emissivity was measured with a TH9100MR thermo tracer. The accuracy of equipment and uncertainties of materials were assumed to be normally distributed and reported with a confidence interval of 95%.

Latin Hypercube Sampling (LHS) was applied as the sampling method in the uncertainty analysis. The input scenarios based on the uncertainty of the main concerned parameters were generated by the LHS sampling method. The LHS sample size was 300. Finally, the Monte

Carlo analysis (MCA) was conducted to perform the total uncertainty on the derived heat flux and CHTC. The resulting uncertainty was given with a confidence interval of 95%.

Table 3. Properties of materials used in the test room.

Material	λ (W/m·K)	ρ (kg/m^3)	C_p (J/kg·K)	ε (-)
Foam	0.038 ± 0.001	14.5 ± 0.1	1500 ± 100	0.96 ± 0.03
Fermcell	0.32 ± 0.01	1150 ± 10	1100 ± 100	0.95 ± 0.03

3.3 Energy balance of the test room

To verify the accuracy of the experiment, the energy balance of the test room is established for designed cases. It is assumed that the heat input into the test room is positive, while the heat removed from the room is negative.

The total convective heat flow equals the total conductive heat flow ($Q_{\mathrm{cond,tot}}$), as radiation heat is only transported from one surface to another ($Q_{\mathrm{rad,tot}}$=0). They can be calculated by Eq. (4) and Eq. (5).

$$Q_{\mathrm{conv,tot}} = \sum_i A_i \cdot q_{\mathrm{conv},i} \tag{4}$$

$$Q_{\mathrm{cond,tot}} = \sum_i A_i \cdot q_{\mathrm{cond},i} \tag{5}$$

The total ventilative heat flow removed for the test room can be determined by the airflow volume rate ($\dot{V}_{air}$), the air density (ρ_{air}), the air heat capacity ($c_{p,air}$), and the temperature difference between the inlet (T_{outlet}) and outlet (T_{inlet}). It can be calculated by Eq. (6).

$$Q_{vent,tot} = \dot{V}_{air} \cdot \rho_{air} \cdot c_{p,air} \cdot (T_{\mathrm{outlet}} - T_{\mathrm{inlet}}) \tag{6}$$

Based on the above equations, the sensible heat balance of the test room can be evaluated by Eq. (7), and the heat unbalance rate is defined as Eq. (8).

$$\Delta Q = Q_{\mathrm{vent,tot}} + Q_{\mathrm{cond,tot}} \tag{7}$$

$$\bar{Q} = \frac{\Delta Q}{Q_{\mathrm{cond,tot}}} \tag{8}$$

Because the jet flowed along with the ceiling, the conductive heat flow in the ceiling was inhomogeneous. Integrating the calculated heat flow of each section to derive the heat flow of the entire ceiling may result in a large error. To estimate the conductive heat flow of the entire ceiling accurately, the linear interpolation and extrapolation methods were used based on the conductive heat flow of each section. Fig. 7 shows the conductive heat flow of the ceiling in case 29 (10 ACH 5 °C Ceiling) after five hours and thirty minutes. The red arrow in Fig. 7 indicates the inlet air direction.

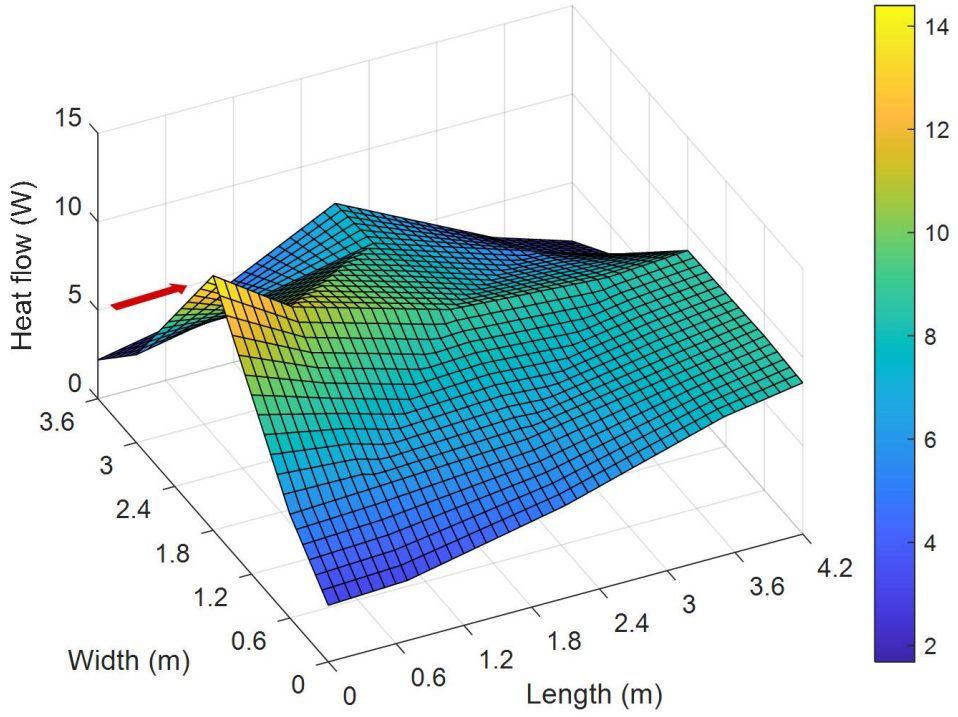

Fig. 7. The conductive heat flow of the ceiling in case 29 after five hours and thirty minutes.

Fig. 8 compares the total ventilative heat flow and total convective heat flow of a representative case (case 29). The two heat flows were in very good agreement. The large initial difference between the two heat flows was due to the thermal capacity of the air in the test room. Fig. 9 shows that during 95% of the cooling period, the uncertainties in $Q_{\mathrm{conv,tot}}$ and $Q_{\mathrm{vent,tot}}$ for case 29, were below ± 15% and ± 4%, respectively. In other cases, a difference of up to 20% over the cooling period (first hour excluded) was found due to experimental errors. While

considering the uncertainties of $Q_{\mathrm{conv,tot}}$ and $Q_{\mathrm{vent,tot}}$, the two flows over the cooling period overlaps.

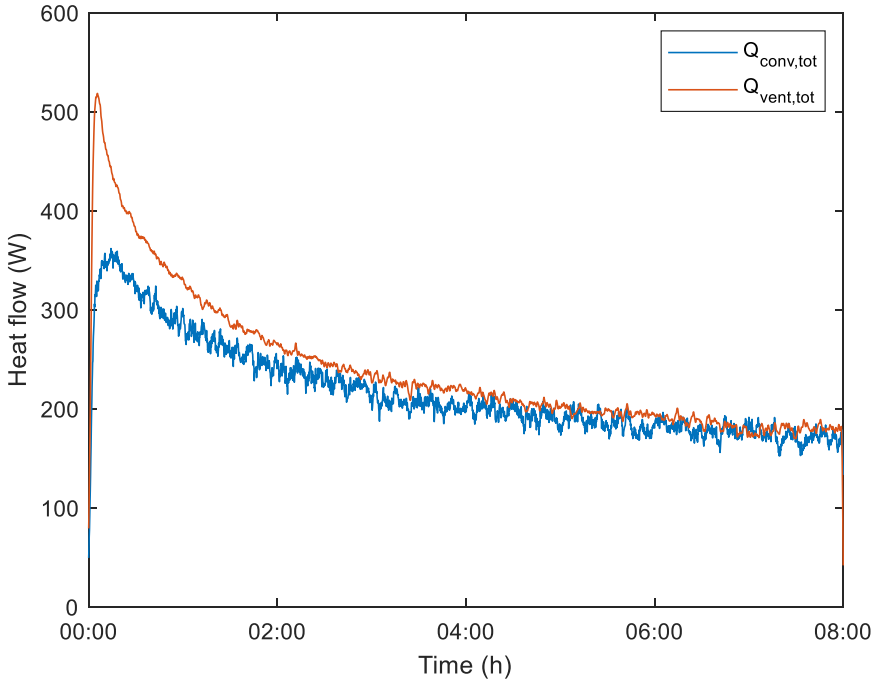

Fig. 8. Total heat flow removed from the room obtained from direct measurements and from integrating the convective heat flows over all surfaces for case 29.

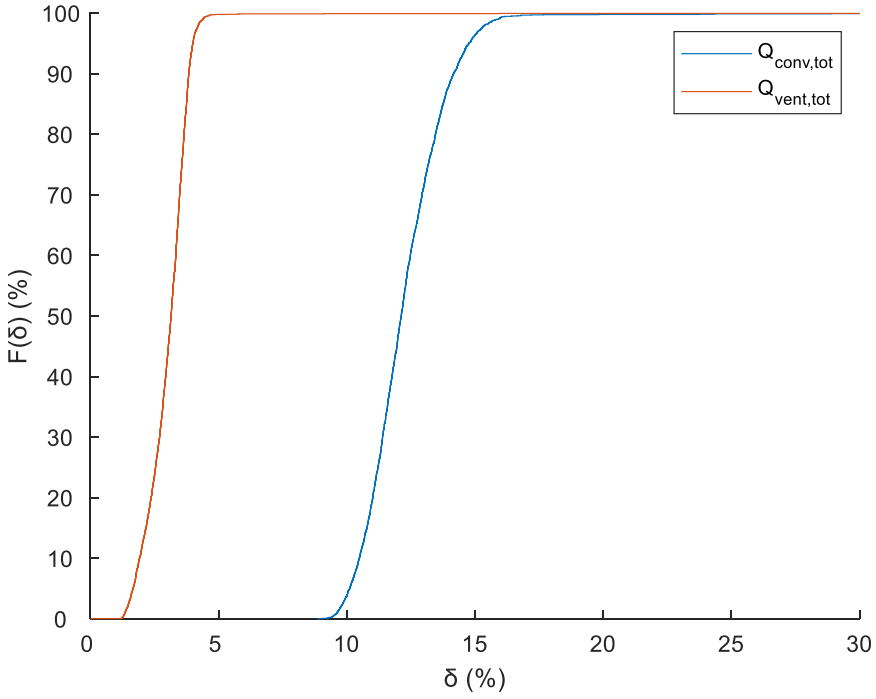

Fig. 9. Cumulative distribution function of the uncertainty in the total ventilative heat flow and total convective heat flow of case 29 due to measurement errors.

3.4 General form of CHTC correlation development

When the forced convection dominates in an enclosure, Eq. (9) shows the relationship between Reynolds number (*Re*) and Nusselt number (*Nu*) for the turbulent flow and laminar flow, respectively [49].

$$Nu = \begin{cases} C_1 \cdot Re^{0.5}, \text{for laminar flow} \\ C_2 \cdot Re^{0.8}, \text{for turbulent flow} \end{cases} \quad (9)$$

where C_1 and C_2 are the constant for different flow patterns, respectively. *Nu* and *Re* in an enclosure can be calculated by Eq. (10) and Eq. (11), respectively.

$$Nu = \frac{hL}{k} \quad (10)$$

$$Re = \frac{\dot{V}}{\nu L} \quad (11)$$

where *h* is the CHTC, *L* is the characteristic length, which can be expressed as the cubic root of the room volume ($V_{room}^{1/3}$). $\dot{V}$, *k* and *v* represent the air volume flow rate, air thermal conductivity, and air dynamic viscosity. Substituting Eq. (9) with (11), the CHTC can also be expressed as a function of $ACH = \dot{V}/V_{room}$ with another constant C_3, by Eq. (12).

$$h = C_3 \cdot ACH^m \quad (12)$$

The exponent *m* is 0.5 for laminar flow, 0.8 for turbulent flow, and between these two values for transitional flow.

Fisher & Pedersen [24] investigated the forced CHTCs in an isothermal room with a radial ceiling diffuser. The supply ACH ranged from 3 to 12 h^{-1}, and the supply air temperature varied between 10 °C to 25 °C. The CHTC proved dependent on the jet mass flow rate rather than the inlet jet velocity and momentum. They then combined the experimental results with Spilter's

experimental results with high ACH from 15 to 100 h^{-1} [22] and developed the CHTC correlations with the turbulent flow pattern in Eq. (12) based on the inlet reference temperature summarized in Table 4.

Table 4. CHTC correlations for the radial ceiling diffuser configuration (ACH: 3 to 100 h^{-1}) [24].

Surface type	**Correlations**
Ceiling	$h = 0.49ACH^{0.8}$
Floor	$h = 0.13ACH^{0.8}$
Walls	$h = 0.19ACH^{0.8}$

Fisher [23] also mentioned that the CHTCs predicted at low flow rates by the correlations in Table 4 did not match the experimental CHTC very well. It may be because the flow pattern was not turbulent, or the inlet jet did not dominate the surface heat transfer at low ACH. Therefore, a modified correlation form for *Nu* and *Re* was developed, as shown in Eq. (13). It can also be transformed into the relationship between *h* and ACH, as shown in Eq. (14).

$$Nu = \mathrm{C}_4 + \mathrm{C}_5 \cdot Re^{0.8} \tag{13}$$

$$h = \mathrm{C}_6 + \mathrm{C}_7 \cdot ACH^{0.8} \tag{14}$$

Table 5 summarizes the CHTC correlations for the radial ceiling diffuser configuration with Eq. (14) for ACH ranges from 3 to 12 h^{-1}.

Table 5. CHTC correlations for the radial ceiling diffuser configuration (ACH: 3 to 12 h^{-1}) [23].

Surface type	**Correlations**
Ceiling	$h = -0.165 + 0.497ACH^{0.8}$
Floor	$h = 0.158 + 0.119ACH^{0.8}$
Walls	$h = -0.198 + 0.195ACH^{0.8}$

Fisher [23] also used a vertical slot located midway up the wall (the sidewall inlet) in an isothermal room to investigate the CHTCs caused by the free horizontal jet, which was summarized in Table 6. The Archimedes number, Ar_e was calculated by Eq. (15).

Table 6. CHTC correlations for the sidewall inlet configuration (ACH: 3 to 12 h^{-1}) [23].

Surface type	Correlations
Ceiling	$h = 0.038 + 599.3ACH^{0.8}/Ar_e$
Floor	$h = 0.698 + 0.173ACH^{0.8}$
Walls	$h = -0.109 + 0.135ACH^{0.8}$

$$Ar_e = \frac{g \cdot \beta \cdot L \cdot (T_{outlet} - T_{inlet})}{\dot{V}} \quad (15)$$

where g is the gravitational acceleration, β is the coefficient of thermal expansion, L is the characteristic length. T_{outlet} and T_{inlet} are the outlet and inlet air temperature, respectively.

The surface flow regime can be assessed by the Richardson number (*Ri*), which is a dimensionless parameter expressed by combining the Grashof number (*Gr*) and *Re*, as shown in Eq. (16).

$$Ri = \frac{Gr}{Re^2} = \frac{g \cdot \beta \cdot (T_{surf} - T_{ref})}{u^2} \cdot \frac{L_{Gr}^3}{L} \quad (16)$$

where u is the airflow speed across the surface, and L_{Gr} is the characteristic length (usually room height) for *Gr*. *Ri* gives the ratio of the buoyant forces over the momentum forces and has been used in BES software such as EnergyPlus to switch the CHTC algorithms between natural, mixed, and forced flow regimes [36]. Typically, forced convection dominates for $Ri < 0.1$, natural convection dominates for $Ri > 10$, and mixed convection exists for $0.1 < Ri < 10$ [50].

Calculating Ri for all cases by Eq. (16), where u was measured and averaged by anemometers 50 mm away from the interior surfaces, and T_{ref} was selected as the indoor air temperature measured and averaged by two thermocouples 1.2 m away from the floor. It can be concluded that for the cases with ACH of 2 h^{-1}, the average *Ri* during the cooling period for different surfaces ranged from 1.9 to 4.9, indicating that natural convection form cannot be neglected at the low ACH. For cases with ACH of 5, 7, and 10 h^{-1}, the average *Ri* for different surfaces were much below or close to 0.1, indicating that forced convection dominated. Thus, considering Eq.

(14) and the meaning of exponent *m* in Eq. (12), the general form for the CHTC correlations developed in this study is shown by Eq. (17).

$$h = C_8 + C_9 \cdot ACH^m, \ 0.5 \le m \le 0.8 \quad (17)$$

The constant C_8, C_9, and the exponent *m* were derived from curve fitting of experimental data. The lower bound and upper bound of *m* are 0.5 and 0.8, respectively. The existing correlations shown in Table 4 and Table 6 were compared with the experimental CHTC. Table 4, instead of Table 5, was selected because the correlations in Table 4 were widely used. Other researchers also developed correlations for forced convection [22][28][51]. However, those correlations were used for the displacement ventilation or selected the outlet reference temperature; thus, those correlations were not considered in this study.

The inlet temperature was selected as the reference temperature to calculate CHTC in this study for the following reasons: (1) the convective heat flow in the room was mainly driven by the inlet airflow, especially the interior surfaces did not have heat gains (e.g., solar radiation on the part of the floor at daytime) at night, (2) the mean indoor air temperature was difficult to determine accurately due to the uneven air distribution, and (3) compared to other temperatures (outlet air temperature, local air temperature, and indoor air temperature), the inlet temperature contributed to the highest temperature difference in Eq. (1), leading to the smallest uncertainty of CHTC.

4 RESULTS AND DISCUSSIONS

4.1 CHTC at the ceiling

4.1.1 Average values

The CHTCs of the nine sections with the inlet temperature as reference at the ceiling were very different due to the high gradient velocity and temperature. However, all CHTCs fluctuated

moderately during the NV period for case 3 (7 ACH 10 °C Ceiling+Floor) (see Fig. 10a). The first hourly data were excluded due to the high uncertainties at the beginning of the experiments. Along the inlet direction, section 4 had the highest CHTC (about 18 $W/m^2 \cdot K$), followed by sections 5 and 6. The CHTCs at the remaining sections were below 2 $W/m^2 \cdot K$. Directly averaging the nine CHTCs may overestimate the CHTC at the entire ceiling. Therefore, the same linear interpolation and extrapolation method introduced in Section 3.3 was adopted to calculate the convective heat flux and surface temperature of the ceiling. After that, Eq. (1) was used to calculate the surface-averaged CHTC over the night cooling period for different cases. Fig. 10b shows an example from case 3 in which the average CHTC at the ceiling was 1.97 $W/m^2 \cdot K$ with a standard deviation of 0.14 $W/m^2 \cdot K$ during the cooling period from 01:00 to 08:00.

The CHTC predicted by Fisher's correlation for the sidewall inlet configuration at the ceiling (cf. Table 6) was also compared with the experimental CHTCs. The results indicate that the correlation for the sidewall inlet configuration at the ceiling largely underestimated the experimental CHTC. Fig. 10b also shows an example from case 3, in which the CHTC calculated by the correlation for the sidewall inlet ranged from 0.25 to 0.4 $W/m^2 \cdot K$, much less than the experimental CHTC over the cooling period. The mismatch may be because the sidewall inlet in Fisher's experiment was located in the midway of the west wall and induced a free horizontal jet, which subsequently did not impact the ceiling sufficiently.

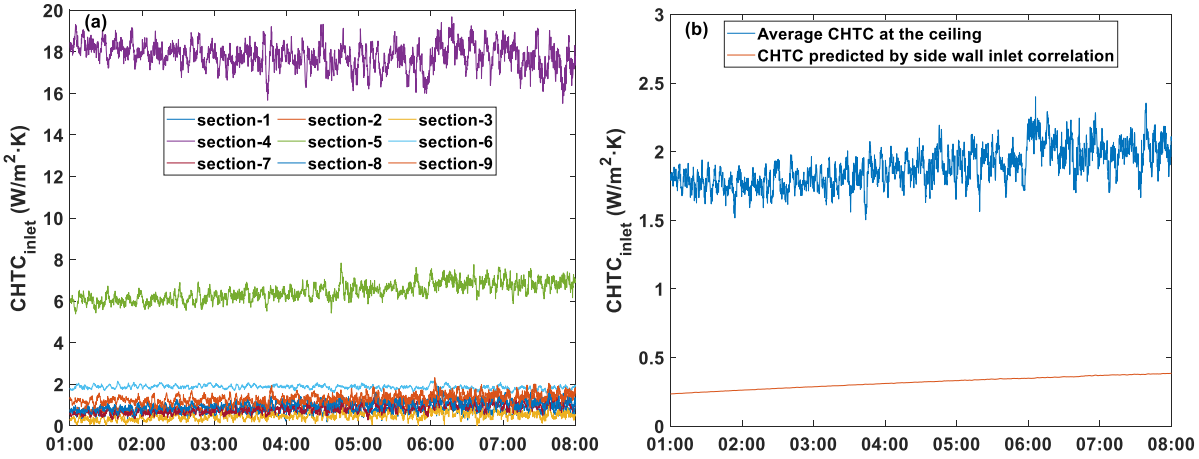

Fig. 10. (a) CHTCs of nine sections at the ceiling, and (b) average CHTC over the ceiling during NV for case 3 (first hourly data excluded).

Fig. 11 shows the experimental surface-averaged CHTCs and fitted curves with R^2 (coefficient of determination) between 0.93 and 0.99 for different designed cases, as well as Fisher & Pedersen's CHTC curve for the ceiling. The fitted curve is deduced by the nonlinear least square method with the trust-region-reflective algorithm [52]. The uncertainties estimated for the average CHTC at the ceiling range from ± 4% to ± 10% for different cases. It should be noticed that the title above the figures corresponds to the thermal mass distribution schemes listed in Table 2. In Fig. 11 a, b and c, the cases with two ΔT_0 (i.e., 5 °C and 10 °C) under the same ACH were for initial trials and had two experimental values. Those values were similar under the same ACH, indicating that CHTC at the ceiling was independent of the ΔT_0. The reason was that the forced convection dominated during NV, which determines that the inlet momentum rather than the temperature difference between the surface and air drives the convective heat transfer. It should be noticed that for the cases with the ACH of 2 h^{-1}, the discrepancy between the two experimental values is a little high (36.7%). This can be explained by the fact that at low ACH, the flow over the ceiling might not be turbulent, which also leads to the value of exponent *m* to the lower bound (i.e., 0.5) for the fitted curves. However, considering that the

absolute difference between the two experimental values at the ACH 2 h^{-1} was only 0.22 $W/m^2 \cdot K$, the prediction error caused by the fitted curve at low ACH should be acceptable.

For most cases, the experimental values were smaller than those predicted by Fisher & Pedersen's correlation. The reason should be that the air jet from the radial ceiling diffuser covered a larger area of the ceiling and the Coanda effect was strong to let the jet attached to the ceiling. For cases shown in Fig. 11f, the existing correlation predicted CHTC relatively well for the experimental values. Consequently, the fitted curve and the existing CHTC curve are in very good agreement. Compared to cases (Fig. 11a to f) where ceiling had thermal mass, the ceiling without thermal mass (Fig. 11g to j) had much lower CHTCs. There are two possible explanations: (1) installing the thermal mass on the original ceiling (i.e., foam boards) provided a larger dynamic heat capacity that can be a heat sink to store/release more heat, or (2) the thermal mass slowed down the congruence of the local air temperature and the surface temperature, resulting in a higher temperature difference for a longer period to release more energy from thermal mass. Comparing the cases that ceiling with thermal mass or without thermal mass also proved that the thermal mass distribution on other interior surfaces affected the average CHTC at the ceiling. The reason was that thermal mass on other surfaces affected the radiative heat transfer between surfaces. However, Fisher & Pedersen's correlations were derived from the isothermal experimental conditions that greatly eliminated the radiative heat transfer inside the enclosure. By comparing the cases with tables (Fig. 11b, c, d), it can be seen that the locations of tables had little impact on the average CHTC at the ceiling.

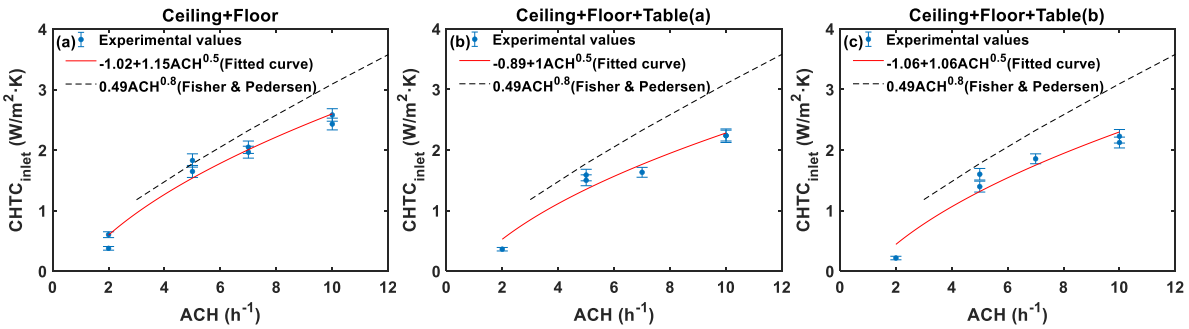

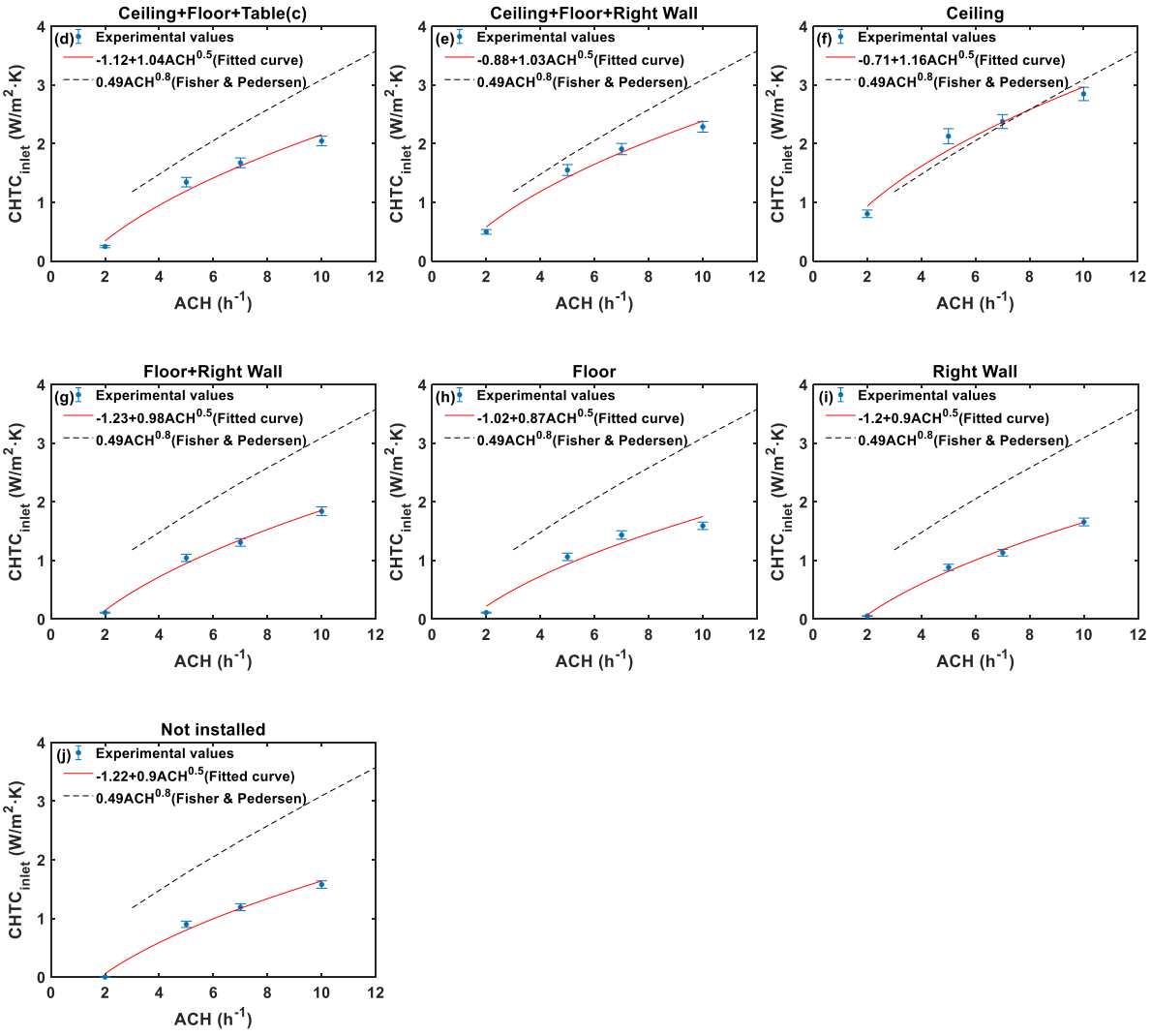

Fig. 11. Average CHTC at the ceiling for (a) thermal mass on the ceiling, (b) ceiling + floor + wall, (c) ceiling, (d) ceiling + floor + table (a), (e) ceiling + floor + table (b), (f) ceiling + floor + table (c), (g) floor + wall, (h) floor, (i) wall, and (j) thermal mass not installed.

4.1.2 Local values

The existing mixed CHTC correlations with local air temperature as reference were also compared with experimental local CHTC. The local air temperatures measured by the thermocouples 50 mm away from the nine sections of the ceiling were selected as the reference temperatures. Fig. 12 shows an example of local CHTCs of nine sections at the ceiling for case 3 (7 ACH 10 °C Ceiling+Floor) after two hours. The CHTC close to the inlet was the highest

and gradually decreased along the length of the ceiling. The ratio between the highest CHTC and the lowest one was about 28.

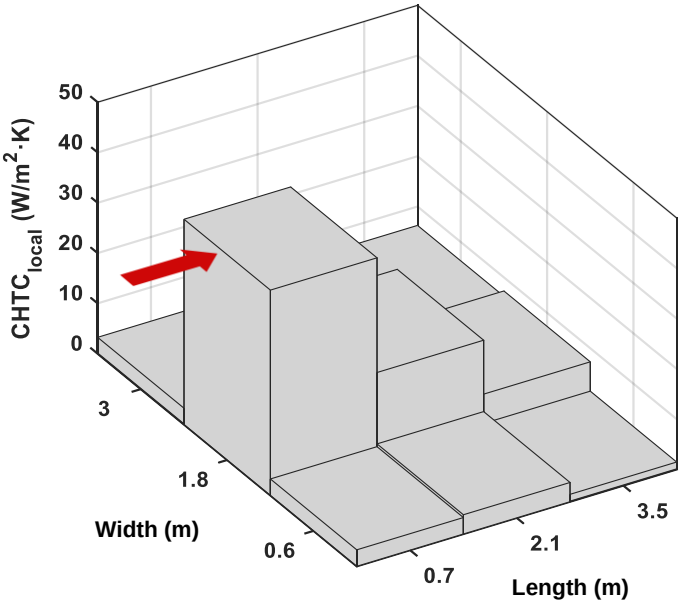

Fig. 12. Local CHTC at the ceiling for case 3 after two hours.

Le Dréau et al. [31] developed a mixed correlation using local velocity, surface temperature, inlet air temperature, and indoor air temperature. We reformulated the correlation using the local air temperature as the indoor air temperature was difficult to be determined accurately and transformed the modified correlation for the entire ceiling by Eq. (18).

$$h_{local,1} = \left[\left(0.6 \cdot \left(\frac{T_{\text{ceiling}} - T_{\text{local}}}{D_h}\right)^{0.2}\right)^6 + \left(\frac{6.02 \cdot u^{0.8}}{D_h^{0.2}}\right)^6 \left(\frac{T_{\text{ceiling}} - T_{\text{inlet}}}{T_{\text{ceiling}} - T_{\text{local}}}\right)^6\right]^{1/6} \quad (18)$$

Moreover, Awbi & Hatton [27] proposed a mixed convection correlation for the ceiling by a fan box with an adjustable nozzle at the end of a heated ceiling by Eq. (19). Novoselac et al. [53] also developed a mixed convection correlation for the ceiling by configuring high aspiration ceiling diffusers with a cooled ceiling by Eq. (20). Both equations selected the local air temperatures as reference temperatures, which were measured 100 mm away from the ceiling.

$$h_{local,2} = \left[\left(0.704 \cdot \frac{\left(T_{\text{ceiling}} - T_{\text{local}}\right)^{0.133}}{D_h^{0.601}}\right)^{3.2} + \left(1.35 \cdot W^{0.074} U^{0.772}\right)^{3.2}\right]^{1/3.2} \quad (19)$$

$$h_{local,3} = \left[\left(0.704 \cdot \frac{\left(T_{\text{ceiling}} - T_{\text{local}}\right)^{0.133}}{D_h^{0.601}}\right)^{3} + \left(2.0 \cdot ACH^{0.39}\right)^{3}\right]^{1/3}, T_{\text{ceiling}} > T_{\text{local}} \quad (20)$$

where T_{ceiling} and T_{local} are the ceiling surface temperature and the local air temperature, respectively. W is the width of the nozzle opening, U is the velocity at nozzle opening, and D_h is the hydraulic diameter of the ceiling, which is calculated by 4×area/perimeter.

The three existing correlations were compared with the experimental local CHTC over the entire ceiling during the night cooling period. The results show that all three existing correlations cannot predict the local CHTC adequately. Fig. 13 shows the local CHTCs for four cases as examples. The CHTC in cases with thermal mass on the ceiling fluctuated more than in cases without thermal mass on the ceiling. The ceiling with thermal mass (Fig. 13a, c) also had higher local CHTC than the ceiling without thermal mass (Fig. 13b, d), especially at low ACH.

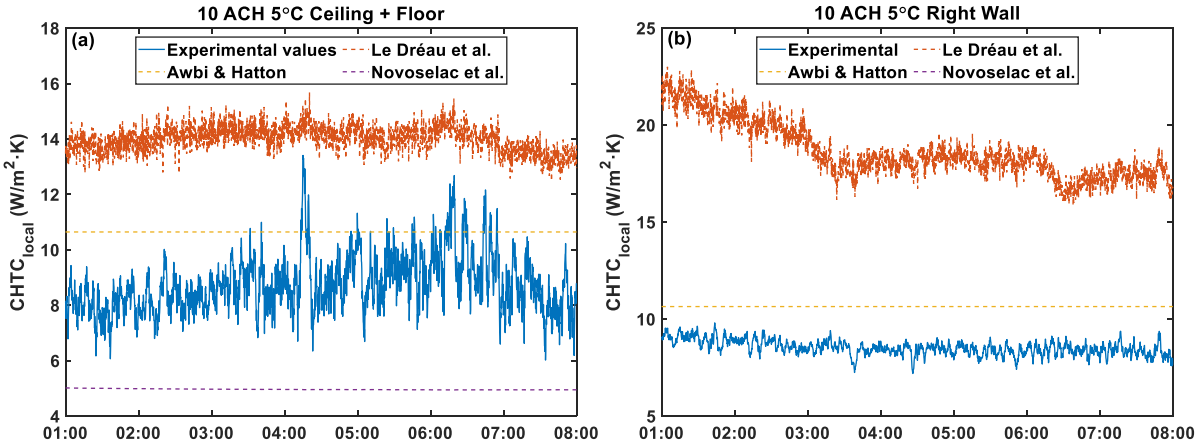

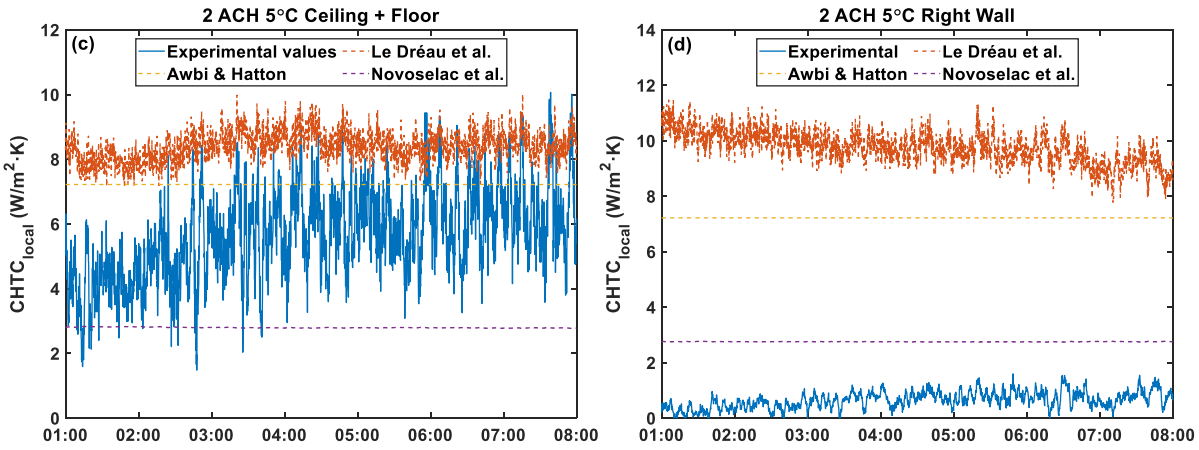

Fig. 13. Local CHTC at the ceiling for (a) case 2, (b) case 41, (c) case 8, and (d) case 44.

4.2 CHTC at the floor

Fig. 14 shows the surface-averaged CHTCs and fitted curves with R^2 between 0.91 and 0.99 for different designed cases, as well as two existing CHTC curves for the floor. The uncertainties estimated for the average CHTC values at the floor ranged from ± 6% to ± 10% for different cases. Like the CHTC at the ceiling, the CHTC at the floor increased when the floor has thermal mass.

Fisher's correlation (i.e., sidewall inlet) predicted higher CHTC at the floor than Fisher & Pedersen's correlation (i.e., radial ceiling diffuser) under the same ACH. The reason was that the free horizontal jet from the vertical slot located in the middle of a west wall covered a larger floor area with a higher air velocity compared to the radial ceiling diffuser. Fisher's correlation predicted CHTC relatively well for the cases with the thermal mass on the floor, especially for cases shown in Fig. 14e, but overestimated the experimental CHTC in cases without thermal mass. In contrast, Fisher & Pedersen's correlation underestimated the experimental values when the floor had thermal mass but gave relatively accurate results for the cases without thermal mass on the floor, especially for the cases in Fig. 14f. By comparing the cases with tables (Fig. 14b, c, d), it can be seen that the locations of tables had little impact on the average CHTC at the floor.

It is worth noticing that the exponent *m* for the floor is 0.8, indicating that flow at the floor was turbulent even at the low ACH, which is demonstrated by the similarity of experimental CHTCs of the cases at 2 ACH with two ΔT_0 in Fig. 14a. One reason why the flows over the ceiling and floor were different at low ACH could be that the inlet air evolved into the free horizontal jet and covered a small ceiling area. Another reason may be that the outlet located at the bottom of the front wall exhausted the air, which resulted in a relatively high local velocity at the floor level. Fig. 15 shows the local air velocity over the ceiling and floor with the linear interpolation and extrapolation method for case 4 (2 ACH 10 °C Ceiling+Floor) after two hours, which further verifies the two reasons mentioned above. The red arrow represents the airflow direction. Furthermore, the CHTC at the floor was higher than the ceiling at low ACH when comparing the same cases in Fig. 14 with Fig. 11, which can also be explained by Fig. 15.

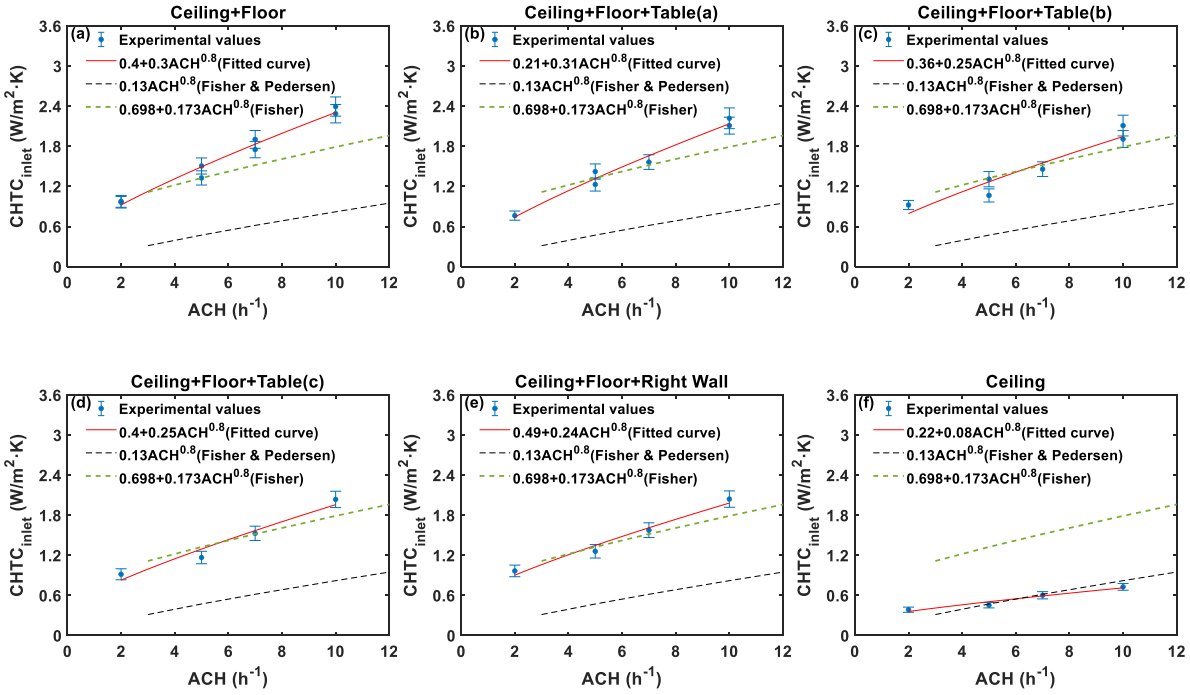

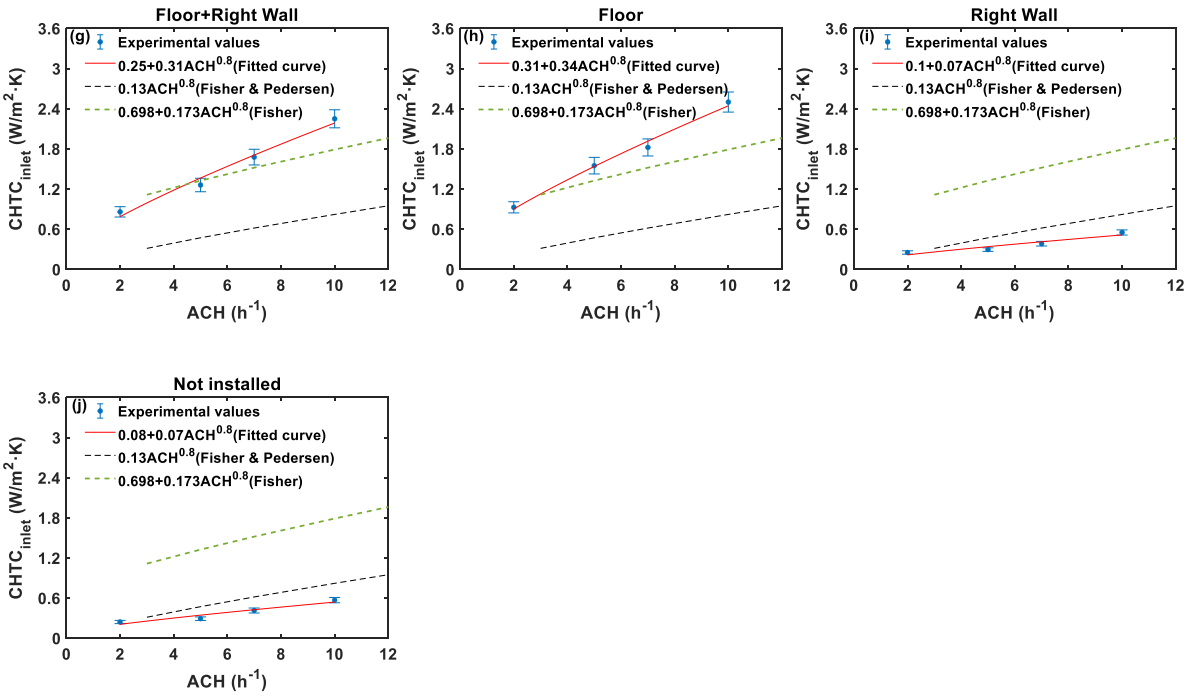

1

2

3 Fig. 14. Average CHTC at the floor for (a) thermal mass on the ceiling, (b) ceiling + floor +
4 wall, (c) ceiling, (d) ceiling + floor + table (a), (e) ceiling + floor + table (b), (f) ceiling +
5 floor + table (c), (g) floor + wall, (h) floor, (i) wall, and (j) thermal mass not installed.

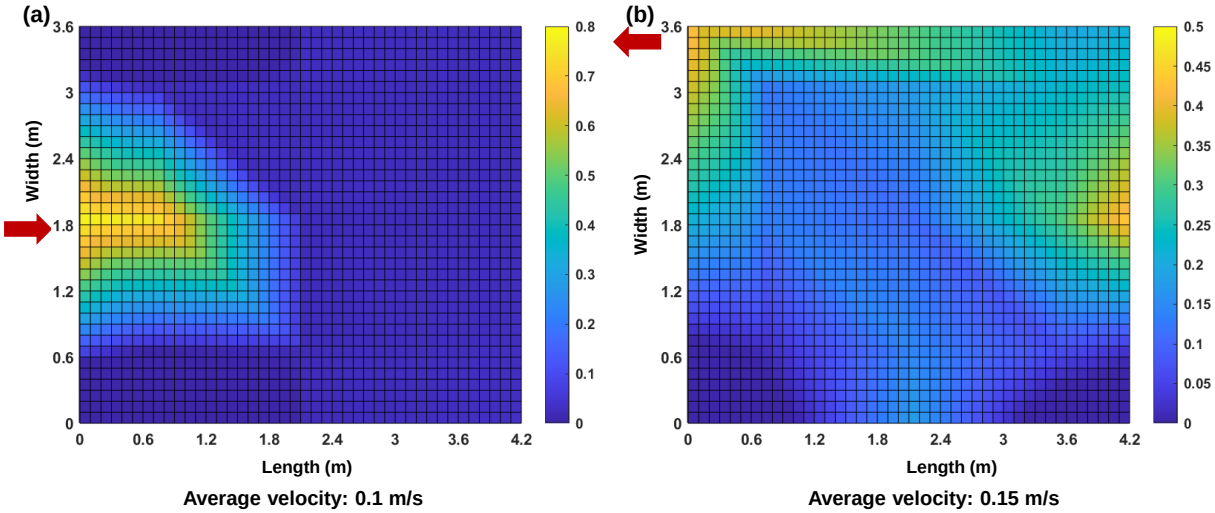

6

7 Fig. 15. Air velocity over the (a) ceiling and (b) floor for case 4 after two hours.

8 **4.3 CHTC at walls**

9 Fig. 16 shows the surface-averaged CHTCs at walls and the two existing CHTC curves for
10 walls. Table 7 shows the fitted curve functions with R^2 between 0.91 and 0.98 for different

designed cases. The uncertainties estimated for the average CHTCs at walls ranged from ± 6% to ± 10% for different cases. Due to the inlet and outlet positions in the experiment, the inlet jet was not evenly distributed in the test room, resulting in different CHTCs at four walls. Contrary to the comparison between the two existing correlations at the floor, Fisher's correlation (i.e., sidewall inlet) predicted lower CHTC at walls than Fisher & Pedersen's correlation (i.e., radial ceiling diffuser) at the same ACH. The reason was that the ceiling jet from the radial ceiling diffuser attached a larger wall area than the free horizontal jet from the middle of a west wall. Both the correlations predicted CHTC well for some specific cases. For instance, Fisher & Pedersen's correlation matched quite well with the experimental CHTCs at the back wall without thermal mass (Fig. 16c). In comparison, Fisher's correlation predicted CHTC well for the front and left walls of cases with the thermal mass on the ceiling, floor, and right wall (Fig. 16a, d).

As shown in Fig. 16b, when the right wall had thermal mass, the CHTC at the right wall almost doubled, compared to the cases where the right wall was without thermal mass. The locations of tables had a small influence on the CHTCs at the walls by comparing the cases with tables and without tables. By comparing the walls without thermal mass, the back wall had the highest CHTCs (Fig. 16c), followed by the right wall (Fig. 16b). One reason was that after the inlet jet flowed away from the ceiling, it hit the back wall before falling onto the floor along the wall. Another reason was that the outlet was located on the right corner of the front wall, which caused the airflow to approach the right wall (cf. Fig. 15b). The front and left walls had similar CHTCs at the same ACH by comparing Fig. 16 a and d. Thus, the corresponding fitted curve functions were similar, as shown in Table 7. It should be noticed that most of the exponent *m* for the back wall were between 0.5 and 0.6 because the back wall was affected relatively less by the inlet jet at the low ACH, which made the flow not turbulent at the back wall.

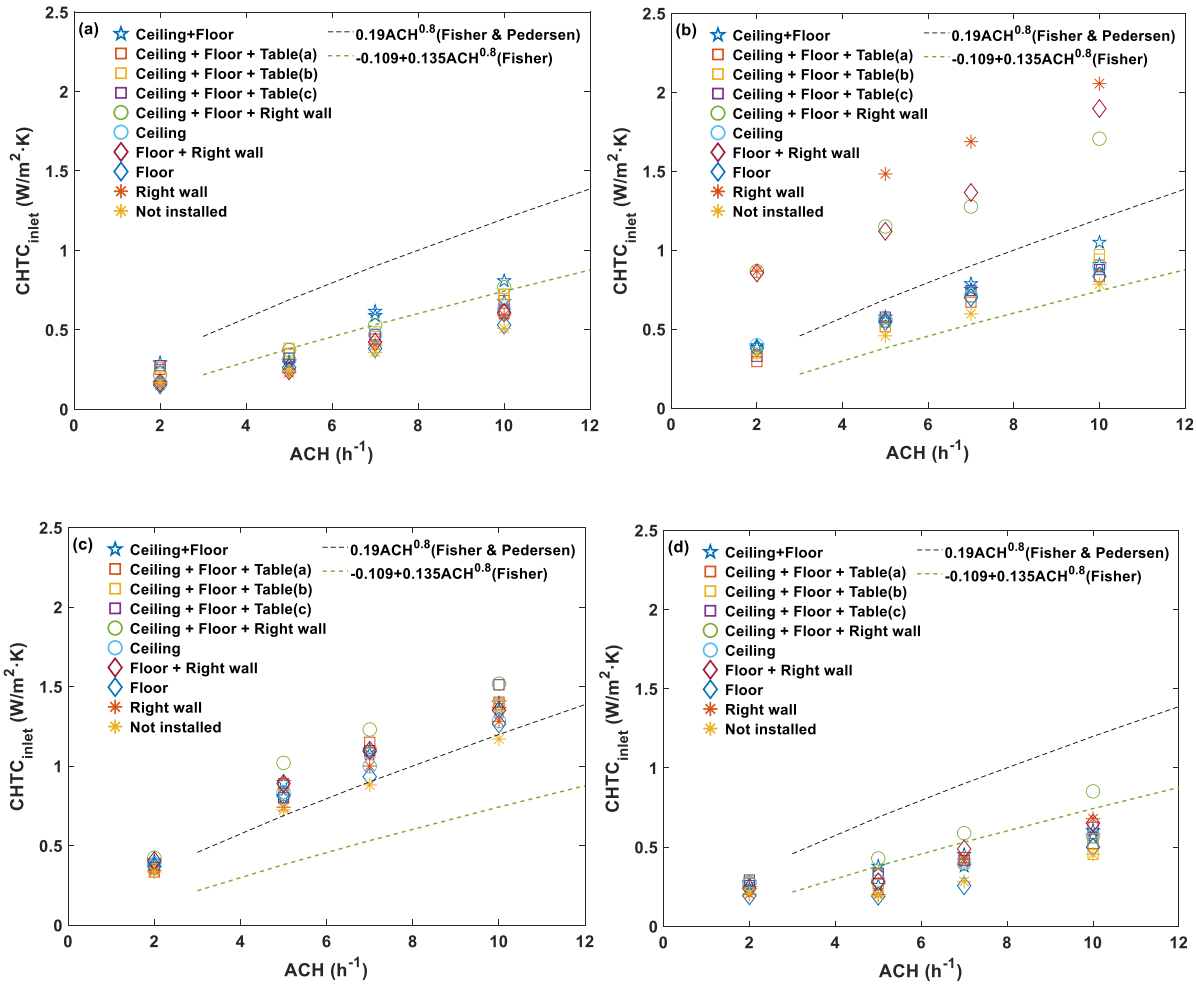

Fig. 16. Average CHTC for the (a) front wall, (b) right wall, (c) back wall, (d) left wall.

Table 7. Fitted curve functions for different walls of designed cases.

Thermal mass distribution	Front wall	Right wall	Back wall	Left wall
Ceiling+Floor	$-0.03+0.12ACH^{0.8}$	$0.14+0.13ACH^{0.8}$	$-0.4+0.56ACH^{0.5}$	$0.1+0.07ACH^{0.8}$
Ceiling+Floor+Table(a)	$0.04+0.09ACH^{0.8}$	$0.07+0.13ACH^{0.8}$	$-0.48+0.6ACH^{0.5}$	$0.1+0.07ACH^{0.8}$
Ceiling+Floor+Table(b)	$0.02+0.11ACH^{0.8}$	$0.07+0.14ACH^{0.8}$	$-0.28+0.42ACH^{0.6}$	$0.11+0.06ACH^{0.8}$
Ceiling+Floor+Table(c)	$0.09+0.08ACH^{0.8}$	$-0.12+0.32ACH^{0.8}$	$-0.09+0.25ACH^{0.8}$	$0.12+0.07ACH^{0.8}$
Ceiling+Floor+Right wall	$-0.02+0.12ACH^{0.8}$	$0.52+0.18ACH^{0.8}$	$-0.43+0.63ACH^{0.5}$	$0.02+0.13ACH^{0.8}$
Ceiling	$-0.03+0.1ACH^{0.8}$	$0.19+0.11ACH^{0.8}$	$-0.33+0.51ACH^{0.5}$	$0.11+0.07ACH^{0.8}$
Floor+Right wall	$-0.05+0.1ACH^{0.8}$	$0.39+0.22ACH^{0.8}$	$-0.35+0.54ACH^{0.5}$	$0.03+0.09ACH^{0.8}$
Floor	$-0.01+0.08ACH^{0.8}$	$0.2+0.1ACH^{0.8}$	$-0.21+0.4ACH^{0.57}$	$0.02+0.06ACH^{0.8}$
Right wall	$-0.05+0.1ACH^{0.8}$	$-0.07+0.67ACH^{0.8}$	$-0.15+0.31ACH^{0.66}$	$-0.07+0.11ACH^{0.8}$
Not installed	$-0.01+0.08ACH^{0.8}$	$0.14+0.1ACH^{0.8}$	$-0.15+0.31ACH^{0.62}$	$0.06+0.05ACH^{0.8}$

4.4 CHTC at tables

As there are no specific CHTC correlations for tables, the indoor furniture is usually regarded as a horizontal and upward-facing surface in BES software [36]. The existing CHTC correlations for the floor were used to compare the experimental CHTCs at tables and the fitted curves. Fig. 17 shows the surface-averaged CHTCs at walls, fitted curves, and corresponding existing CHTC correlations. The uncertainties estimated for the average CHTCs at tables ranged from 4% to 9% for different cases. Compared to Fisher's correlation that underestimated all experimental CHTCs, Fisher & Pedersen's correlation predicted CHTC relatively well for many cases.

Each table has two sides (surfaces facing upward and downward), and the two sides had different CHTCs due to the different air distribution above the surfaces. When comparing the CHTC at the same table surface with different locations, the locations of tables and air distribution had different influences on the value of CHTC. For instance, the CHTCs at table 2 surface facing upward were quite different at different locations, whereas the opposite was true for table 3 surface facing downward. It can seem surprising that the CHTCs at upward-facing surfaces of tables under 2 ACH were larger than at higher ACH, especially for tables in the middle of the room (Table(a), Fig. 2a). The reason was that, at 2ACH, the inlet jet flowed from the ceiling and fell onto the tables located in the middle of the room (cf. Fig. 15a), resulting in a higher airflow velocity and a larger area affected at the upward-facing surfaces. Thus, the CHTCs at 2 ACH of "Table(a)" location were not involved in the curve fitting.

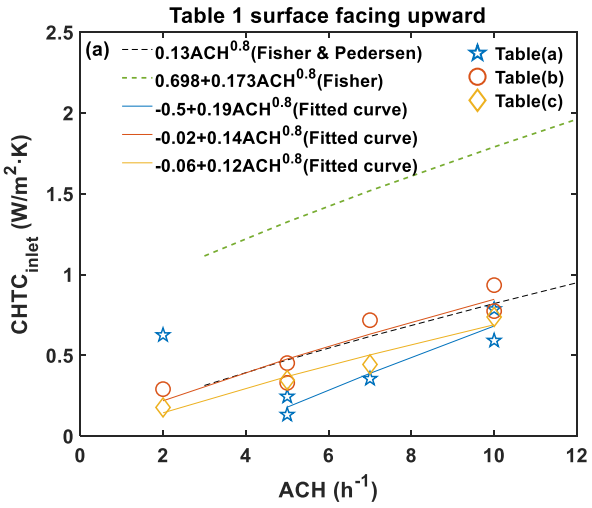
Table 1 surface facing upward
(a)
0.13ACH^0.8(Fisher & Pedersen)
0.698+0.173ACH^0.8(Fisher)
-0.5+0.19ACH^0.8(Fitted curve)
-0.02+0.14ACH^0.8(Fitted curve)
-0.06+0.12ACH^0.8(Fitted curve)
Table(a)
Table(b)
Table(c)
CHTC_inlet (W/m^2·K)
ACH (h^-1)

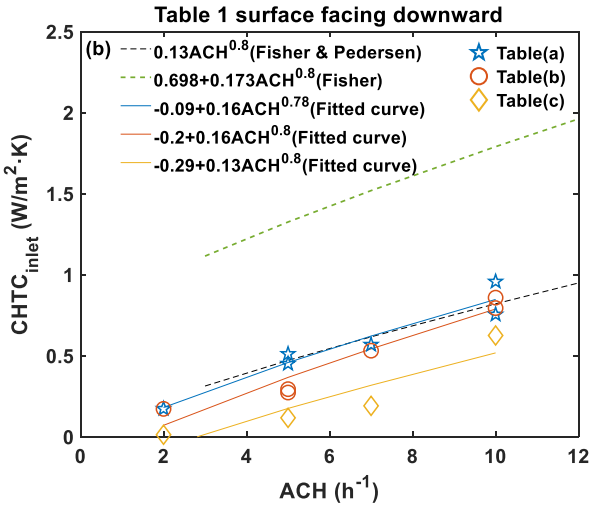
Table 1 surface facing downward
(b)
0.13ACH^0.8(Fisher & Pedersen)
0.698+0.173ACH^0.8(Fisher)
-0.09+0.16ACH^0.78(Fitted curve)
-0.2+0.16ACH^0.8(Fitted curve)
-0.29+0.13ACH^0.8(Fitted curve)
Table(a)
Table(b)
Table(c)
CHTC_inlet (W/m^2·K)
ACH (h^-1)

1

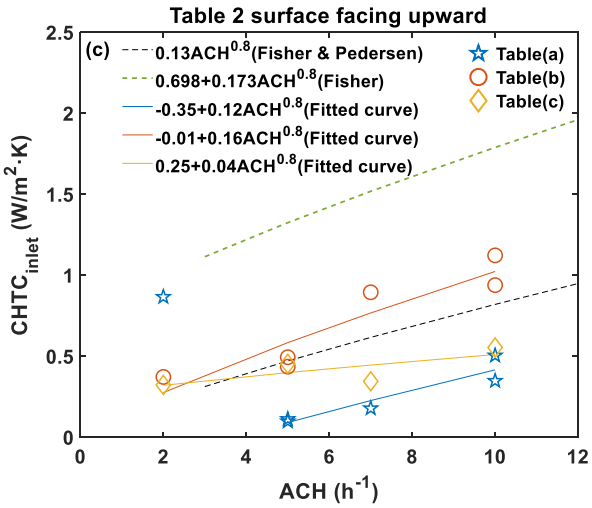
Table 2 surface facing upward
(c)
0.13ACH^0.8(Fisher & Pedersen)
0.698+0.173ACH^0.8(Fisher)
-0.35+0.12ACH^0.8(Fitted curve)
-0.01+0.16ACH^0.8(Fitted curve)
0.25+0.04ACH^0.8(Fitted curve)
Table(a)
Table(b)
Table(c)
CHTC_inlet (W/m^2·K)
ACH (h^-1)

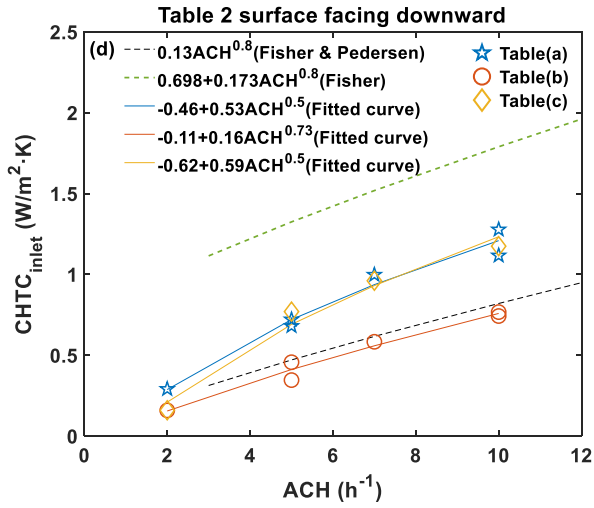
Table 2 surface facing downward
(d)
0.13ACH^0.8(Fisher & Pedersen)
0.698+0.173ACH^0.8(Fisher)
-0.46+0.53ACH^0.5(Fitted curve)
-0.11+0.16ACH^0.73(Fitted curve)
-0.62+0.59ACH^0.5(Fitted curve)
Table(a)
Table(b)
Table(c)
CHTC_inlet (W/m^2·K)
ACH (h^-1)

2

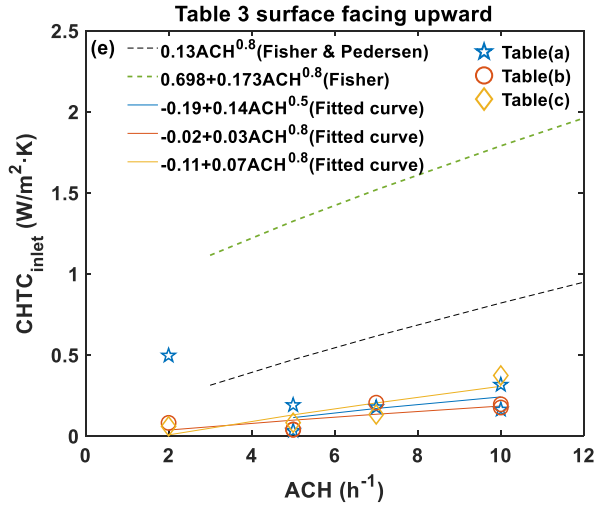
Table 3 surface facing upward
(e)
0.13ACH^0.8(Fisher & Pedersen)
0.698+0.173ACH^0.8(Fisher)
-0.19+0.14ACH^0.5(Fitted curve)
-0.02+0.03ACH^0.8(Fitted curve)
-0.11+0.07ACH^0.8(Fitted curve)
Table(a)
Table(b)
Table(c)
CHTC_inlet (W/m^2·K)
ACH (h^-1)

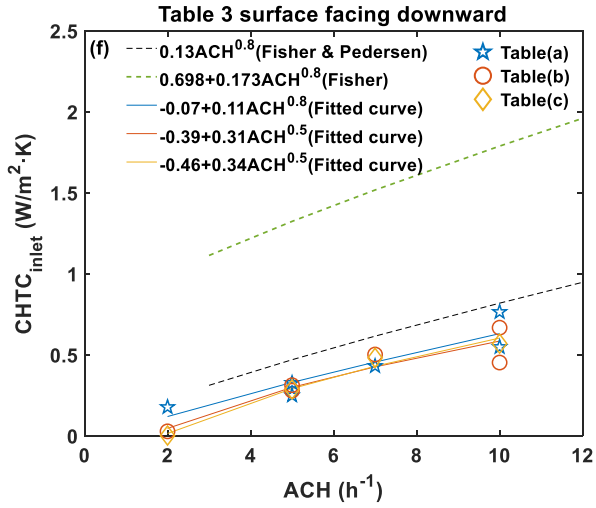
Table 3 surface facing downward
(f)
0.13ACH^0.8(Fisher & Pedersen)
0.698+0.173ACH^0.8(Fisher)
-0.07+0.11ACH^0.8(Fitted curve)
-0.39+0.31ACH^0.5(Fitted curve)
-0.46+0.34ACH^0.5(Fitted curve)
Table(a)
Table(b)
Table(c)
CHTC_inlet (W/m^2·K)
ACH (h^-1)

3

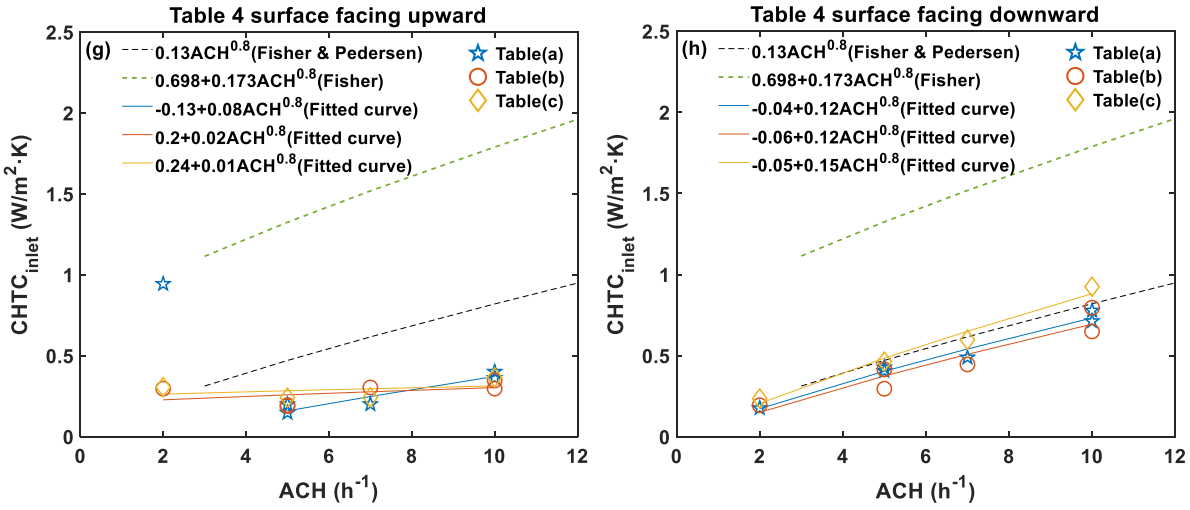

Fig. 17. Average CHTC at different table surfaces.

4.5 Mean CHTC of the test room

The mean CHTC of the test room $h_{\text{mean}} = q_{\text{conv,tot}} / (T_{\text{surf,mean}} - T_{\text{inlet}})$ was also investigated. Fig 18 shows the linear relationship between the hourly total convective heat flux ($q_{\text{conv,tot}}$) and the temperature difference between the mean interior surfaces and the inlet air ($T_{\text{surf,mean}} - T_{\text{inlet}}$) of cases 1 to 8 (i.e., thermal mass on the ceiling and floor). The first hourly data were excluded. The convective heat flux decreases with the reduction of the temperature difference. The mean CHTC of the room is not correlated to ΔT_0 but positively correlated to ACH. The reason is that the forced convection dominates during the night cooling; therefore, the inlet temperature has little effect on the mean CHTC of the test room.

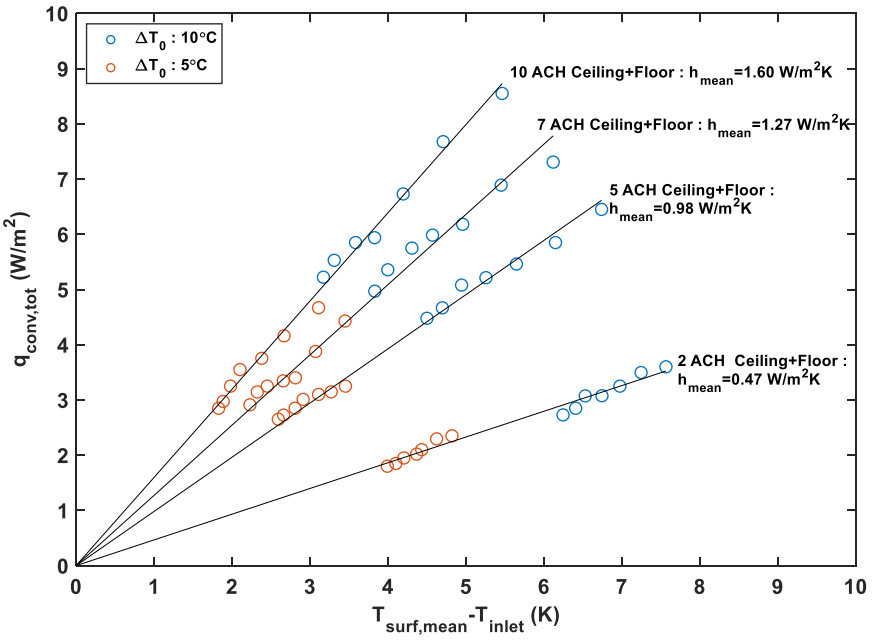

Fig. 18. Mean CHTCs of the test room for cases 1 to 8.

Fig. 19 shows the mean CHTCs with R^2 between 0.94 and 0.98 for 10-ACH cases under different thermal mass distribution schemes. The uncertainties estimated for those mean values were ± 5% for different cases. The mean CHTCs of three cases with tables (Fig. 19, c, and d) were close to each other, indicating that the location of tables had little influence. While comparing the cases with tables with the first case (Fig. 19a) without tables, it can be seen that tables reduced the mean CHTC of the room. One possible reason was that the horizontal tables above the floor did not contribute more heat removed by NV than the sole floor. Another reason may be that the tables enlarged the total interior surface area, increasing the temperature difference ($T_{\text{surf,mean}} - T_{\text{inlet}}$). Apart from the cases with tables, the remaining figures reveal that the mean CHTC of case 25 (Fig. 19e) was the highest (1.67 W/m^2·K), while case 45 (Fig. 19j) had the lowest mean CHTC (0.88 W/m^2·K). The mean CHTC tends to increase with the thermal mass level when the thermal mass is installed on the surfaces.

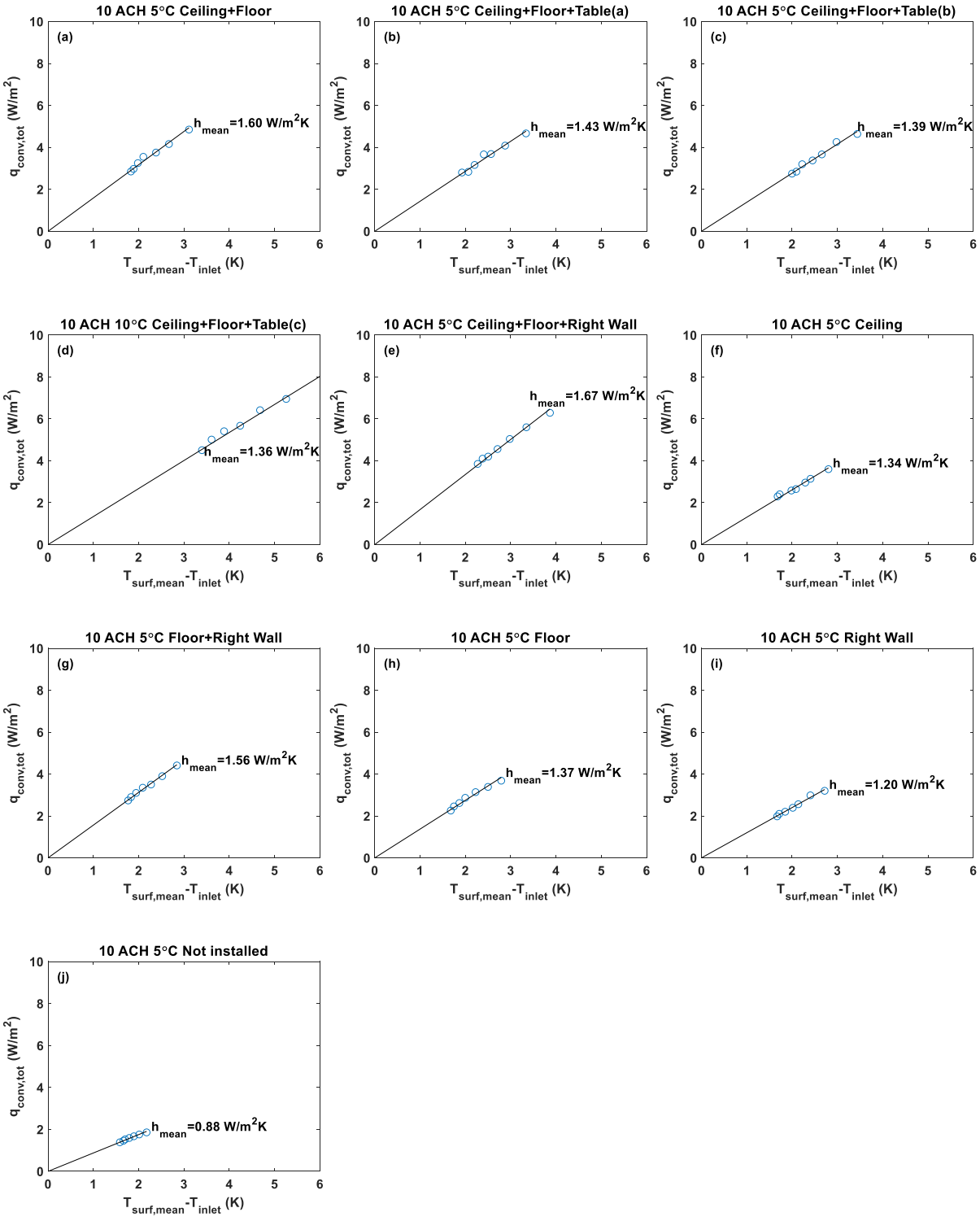

Fig. 19. Mean CHTC of room for (a) case 2, (b) case 9, (c) case 15, (d) case 21, (e) case 25, (f) case 29, (g) case 33, (h) case 37, (i) case 41, and (j) case 45.

5 CONCLUSIONS

This study analyzed dynamic full-scale experiments conducted in a test room with 10 thermal mass distribution schemes, which were cooled down by four constant air change rates per hour (ACH) and two inlet air temperatures for eight hours to simulate night cooling with mixing ventilation. The surface-averaged convective heat transfer coefficient (CHTC) at interior surfaces and local CHTC at the ceiling were derived from the experiment and compared with existing correlations. The mean CHTC of the test room was also calculated to investigate the impact of thermal mass, ACH, and inlet temperature. New correlations based on the experimental surface-averaged CHTCs were specifically developed for night ventilation.

The existing CHTC correlations did not accurately predict the average CHTC with the inlet temperature as reference at room interior surfaces for most designed cases, but only relatively well for a few cases. The existing local CHTC correlations also cannot give accurate results to the experimental local CHTC at the ceiling. The installation of thermal mass (i.e., fiber plasterboard) on one original surface with foam boards can significantly enhance its surface-averaged CHTC and affect the average CHTC at other surfaces due to radiative heat transfer. The presence and locations of tables had little influence on the CHTCs at the interior surfaces of the room but may greatly impact the CHTC at table surfaces due to the air distribution.

The mean CHTC of the test room with the inlet temperature as reference was not correlated to the inlet temperature but positively correlated to the ACH. When the thermal mass was installed on the room interior surfaces, a higher thermal mass level induced a higher mean CHTC. If tables were placed in the room, the mean CHTC decreased. The location of tables made no difference in the mean CHTC.

The developed correlations of this study can be adopted to build energy simulation (BES) tools, allowing users to set custom equations for interior surface CHTC to estimate mechanical or

natural night ventilation performance accurately. These correlations also provide the potential to optimize the ACH and thermal mass distribution to improve the night ventilation performance by yearly BES without coupling complex computational fluid dynamics (CFD) methods.

6 ACKNOWLEDGEMENTS

The project is carried out as part of IEA EBC Annex 80 Resilient Cooling. The first author gratefully acknowledges the financial support from the Chinese Scholarship Council (CSC No. 201706050001). The first author would also like to thank Lars Isbach Poulsen, Yanmin Wang, Bolong Wei, Baoming Su, Weiheng Zhang, and Min Liu for their great technical support. We would also like to thank Vivi Søndergaard for her help.

7 REFERENCES

[1] M. Kolokotroni, P. Heiselberg, Ventilative Cooling: State-of-the-Art Review, Aalborg Univ. Aalborg, Denmark. (2015). https://www.buildup.eu/en/node/52462.

[2] E. Solgi, Z. Hamedani, R. Fernando, H. Skates, N.E. Orji, A literature review of night ventilation strategies in buildings, Energy Build. 173 (2018) 337–352. doi:10.1016/j.enbuild.2018.05.052.

[3] S.P. Corgnati, A. Kindinis, Thermal mass activation by hollow core slab coupled with night ventilation to reduce summer cooling loads, Build. Environ. 42 (2007) 3285–3297. doi:10.1016/j.buildenv.2006.08.018.

[4] D.P. Albuquerque, N. Mateus, M. Avantaggiato, G. Carrilho da Graça, Full-scale measurement and validated simulation of cooling load reduction due to nighttime natural ventilation of a large atrium, Energy Build. 224 (2020) 110233. doi:10.1016/j.enbuild.2020.110233.

[5] M. Lança, P.J. Coelho, J. Viegas, Enhancement of heat transfer in office buildings during night cooling − reduced scale experimentation, Build. Environ. 148 (2019) 653–667. doi:10.1016/j.buildenv.2018.11.033.

[6] L.-X.X. Wu, J.-N.N. Zhao, Z.-J.J. Wang, Night ventilation and active cooling coupled operation for large supermarkets in cold climates, Energy Build. 38 (2006) 1409–1416.

doi:10.1016/j.enbuild.2006.02.011.
[7] R. Guo, Y. Gao, C. Zhuang, P. Heiselberg, R. Levinson, X. Zhao, D. Shi, Optimization of cool roof and night ventilation in office buildings: A case study in Xiamen, China, Renew. Energy. 147 (2020) 2279–2294. doi:10.1016/j.renene.2019.10.032.
[8] M. Kolokotroni, A. Aronis, Cooling-energy reduction in air-conditioned offices by using night ventilation, Appl. Energy. 63 (1999) 241–253. doi:10.1016/S0306-2619(99)00031-8.
[9] V. Geros, M. Santamouris, A. Tsangrasoulis, G. Guarracino, Experimental evaluation of night ventilation phenomena, Energy Build. 29 (1999) 141–154. doi:10.1016/S0378-7788(98)00056-5.
[10] P. Blondeau, M. Spérandio, F. Allard, Night ventilation for building cooling in summer, Sol. Energy. 61 (1997) 327–335. doi:10.1016/S0038-092X(97)00076-5.
[11] Z. Wang, L. Yi, F. Gao, Night ventilation control strategies in office buildings, Sol. Energy. 83 (2009) 1902–1913. doi:10.1016/j.solener.2009.07.003.
[12] H. Sha, D. Qi, Investigation of Mechanical Ventilation for Cooling in High-Rise Buildings, Energy Build. 228 (2020) 110440. doi:10.1016/j.enbuild.2020.110440.
[13] W. Ji, Q. Luo, Z. Zhang, H. Wang, T. Du, P.K. Heiselberg, Investigation on thermal performance of the wall-mounted attached ventilation for night cooling under hot summer conditions, Build. Environ. 146 (2018) 268–279. doi:10.1016/j.buildenv.2018.10.002.
[14] E. Solgi, Z. Hamedani, R. Fernando, B. Mohammad Kari, H. Skates, A parametric study of phase change material behaviour when used with night ventilation in different climatic zones, Build. Environ. 147 (2019) 327–336. doi:10.1016/j.buildenv.2018.10.031.
[15] A. O'Donnavan, A. Belleri, F. Flourentzou, G.-Q. Zhang, G.C. da Graca, H. Breesch, M. Justo-Alonso, M. Kolokotroni, M.Z. Pomianowski, P. O'Sullivan, others, Ventilative Cooling Design Guide: Energy in Buildings and Communities Programme. March 2018, Aalborg University, Department of Civil Engineering, 2018. https://venticool.eu/wp-content/uploads/2016/11/VC-Design-Guide-EBC-Annex-62-March-2018.pdf (accessed April 15, 2019).
[16] N. Artmann, H. Manz, P. Heiselberg, Parameter study on performance of building cooling by night-time ventilation, Renew. Energy. 33 (2008) 2589–2598. doi:10.1016/j.renene.2008.02.025.
[17] R. Guo, Y. Hu, M. Liu, P. Heiselberg, Influence of design parameters on the night ventilation performance in office buildings based on sensitivity analysis, Sustain. Cities

Soc. 50 (2019) 101661. doi:10.1016/j.scs.2019.101661.
[18] K. Goethals, H. Breesch, A. Janssens, Sensitivity analysis of predicted night cooling performance to internal convective heat transfer modelling, Energy Build. 43 (2011) 2429–2441. doi:10.1016/j.enbuild.2011.05.033.
[19] ASHRAE, ASHRAE Handbook Fundamentals 2017, in: ASHRAE Handb., 2017. https://www.ashrae.org/technical-resources/ashrae-handbook/description-2017-ashrae-handbook-fundamentals.
[20] T.C. Min, L.F. Schutrum, G. V Parmelee, J.D. Vouris, Natural convection and radiation in a panel heated room, ASHRAE Trans. 62 (1956) 337–358.
[21] F. Alamdari, G.P. Hammond, Improved data correlations for buoyancy-driven convection in rooms, SAGE PublicationsSage UK: London, England, 1983. doi:10.1177/014362448300400304.
[22] J.D. Spitler, C.O. Pedersen, D.E. Fisher, Interior convective heat transfer in buildings with large ventilative flow rates, in: ASHRAE Trans., 1991: pp. 505–515. www.hvac.okstate.edu (accessed May 11, 2020).
[23] D.E. Fisher, An experimental investigation of mixed convection heat transfer in a rectangular enclosure, University of Illinois at Urbana-Champaign, 1995. https://www.ideals.illinois.edu/handle/2142/22513.
[24] D.E. Fisher, C.O. Pedersen, Convective heat transfer in building energy and thermal load calculations, ASHRAE Trans. 103 (1997) 137–148. https://citeseerx.ist.psu.edu/viewdoc/download?doi=10.1.1.616.9820&rep=rep1&type=pdf.
[25] H.B. Awbi, A. Hatton, Natural convection from heated room surfaces, Energy Build. 30 (1999) 233–244. doi:10.1016/S0378-7788(99)00004-3.
[26] I. Beausoleil-Morrison, The adaptive coupling of heat and air flow modelling within dynamic whole-building simulation, 2000. http://www.esru.strath.ac.uk/Documents/PhD/beausoleil-morrison_thesis.pdf (accessed May 13, 2020).
[27] H.B. Awbi, A. Hatton, Mixed convection from heated room surfaces, Energy Build. 32 (2000) 153–166. doi:10.1016/S0098-8472(99)00063-5.
[28] A. Novoselac, B.J. Burley, J. Srebric, Development of new and validation of existing convection correlations for rooms with displacement ventilation systems, Energy Build. 38 (2006) 163–173. doi:10.1016/j.enbuild.2005.04.005.
[29] I. Beausoleil-Morrison, The adaptive simulation of convective heat transfer at internal

building surfaces, Build. Environ. 37 (2002) 791–806. doi:10.1016/S0360-1323(02)00042-2.

[30] N. Artmann, R.L. Jensen, H. Manz, P. Heiselberg, Experimental investigation of heat transfer during night-time ventilation, Energy Build. 42 (2010) 366–374. doi:10.1016/j.enbuild.2009.10.003.

[31] J. Le Dréau, P. Heiselberg, R.L. Jensen, Experimental investigation of convective heat transfer during night cooling with different ventilation systems and surface emissivities, Energy Build. 61 (2013) 308–317. doi:10.1016/j.enbuild.2013.02.021.

[32] D. Olsthoorn, F. Haghighat, A. Moreau, G. Lacroix, Abilities and limitations of thermal mass activation for thermal comfort, peak shifting and shaving: A review, Build. Environ. 118 (2017) 113–127. doi:10.1016/J.BUILDENV.2017.03.029.

[33] K. Goethals, M. Delghust, G. Flamant, M. De Paepe, A. Janssens, Experimental investigation of the impact of room/system design on mixed convection heat transfer, Energy Build. 49 (2012) 542–551. doi:10.1016/j.enbuild.2012.03.017.

[34] P. Wallentén, Convective heat transfer coefficients in a full-scale room with and without furniture, Build. Environ. 36 (2001) 743–751. doi:10.1016/S0360-1323(00)00070-6.

[35] H. Johra, P. Heiselberg, Influence of internal thermal mass on the indoor thermal dynamics and integration of phase change materials in furniture for building energy storage: A review, Renew. Sustain. Energy Rev. 69 (2017) 19–32. doi:10.1016/j.rser.2016.11.145.

[36] U.S. DoE, Energyplus engineering reference, 2020. https://bigladdersoftware.com/epx/docs/9-3/engineering-reference/.

[37] ISO 8990-1996: Thermal insulation — Determination of steady-state thermal transmission properties — Calibrated and guarded hot box, International Standard, (1996). https://www.iso.org/standard/16519.html.

[38] S. Leenknegt, R. Wagemakers, W. Bosschaerts, D. Saelens, Improving the modelling of surface convection during natural night ventilation in building energy simulation models, Proc. Build. Simul. 2011 12th Conf. Int. Build. Perform. Simul. Assoc. (2011) 2233–2240. https://limo.libis.be/primo-explore/fulldisplay?docid=LIRIAS1565328&context=L&vid=Lirias&search_scope=Lirias&tab=default_tab&lang=en_US&fromSitemap=1 (accessed September 26, 2020).

[39] About FTMU Lindab.dk, (n.d.). http://www.lindab.com/dk/pro/products/Pages/FTMU.aspx (accessed July 25, 2020).

[40] J. Le Dreau, P. Heiselberg, R.L. Jensen, Experimental data from a full-scale facility

investigating radiant and convective terminals: Uncertainty and sensitivity analysis, Description of the experimental data, Department of Civil Engineering, Aalborg University, 2014. http://vbn.aau.dk/en/publications/experimental-data-from-a-fullscale-facility-investigating-radiant-and-convective-terminals(1ce46b33-cfa8-4979-b112-cd9ab487f9c7).html (accessed October 22, 2020).

[41] M.H. Kristensen, J.S. Jensen, R.L. Jensen, Air Temperature Measurements Using Dantec Draught Probes, Department of Civil Engineering, Aalborg University, 2015. https://vbn.aau.dk/en/publications/air-temperature-measurements-using-dantec-draught-probes (accessed July 25, 2020).

[42] N. Artmann, R. Vonbank, R.L. Jensen, Temperature measurements using type K thermocouples and the Fluke Helios Plus 2287A data logger thermocouples and the Fluke Helios Plus, 2008.

[43] R.L. Jensen, O.K. Larsen, C.-E. Hyldgård, On the Use of Hot-Sphere Anemometers in a Highly Transient Flow in a Double-Skin Facade, Int. Conf. Air Distrib. Rooms, Roomvent. (2007) 13–15. https://vbn.aau.dk/en/publications/on-the-use-of-hot-sphere-anemometers-in-a-highly-transient-flow-i (accessed July 22, 2020).

[44] EN ISO 13786, Thermal performance of building components – Dynamic thermal characteristics – Calculation methods, (2017). https://webshop.ds.dk/Default.aspx?ID=219&GroupID=91.120.10&ProductID=M289824.

[45] G.D. Smith, Numerical solution of partial differential equations: finite difference methods, Oxford university press, 1985. https://anujitspenjoymath.files.wordpress.com/2019/02/g.-d.-smith-numerical-solution-of-partial-differential-equations_-finite-difference-methods.pdf.

[46] A.J. Chapman, Fundamentals of heat transfer, Macmillan, 1987.

[47] J.R. Ehlert, T.F. Smith, View factors for perpendicular and parallel rectangular plates, J. Thermophys. Heat Transf. 7 (1993) 173–175. doi:10.2514/3.11587.

[48] G. Walton, Calculation of obstructed view factors by adaptive integration, Gaithersburg, MD, 2002. doi:10.6028/NIST.IR.6925.

[49] A. Bejan, Convection heat transfer, John wiley & sons, 2013. https://ebookcentral.proquest.com/lib/aalborguniv-ebooks/detail.action?docID=1161535&pq-origsite=primo.

[50] S. Leenknegt, D. Saelens, Assessing convection modelling in Building Energy Simulation models for night cooling, in: Proc. BS2013 13th Conf. Int. Build. Perform.

Simul. Assoc. Chambery, Fr. August. 2013, 2010: pp. 1160–1167. http://www.ibpsa.org/proceedings/BS2013/p_987.pdf (accessed April 15, 2019).

[51] Novoselac Atila, Combined airflow and energy simulation program for building mechanical system design, 2005. http://www.ce.utexas.edu/prof/Novoselac/Atila_Novoselac_thesis.pdf (accessed May 13, 2020).

[52] Mathworks®, Curve Fitting Toolbox™: User's Guide (R2019b), 2019. https://www.mathworks.com/help/curvefit/.

[53] A. Novoselac, B.J. Burley, J. Srebric, New convection correlations for cooled ceiling panels in room with mixed and stratified airflow, HVAC R Res. 12 (2006) 279–294. doi:10.1080/10789669.2006.10391179.